UNIVERSIDAD DE CONCEPCIÓN
FACULTAD DE INGENIERÍA
DEPARTAMENTO DE INGENIERÍA CIVIL

NUMERICAL SIMULATION OF THE DYNAMIC RESPONSE OF GRANULAR SOILS BY MEANS OF THE DISCRETE ELEMENT METHOD (DEM)

BY

Margarita León Arriagada

Memoria de Título presentada a la Facultad de Ingeniería de la Universidad de Concepción para optar al título de Ingeniero Civil

Profesor Guía
Dr. Gonzalo Montalva Alvarado

Profesional Supervisor
Dr. Andrés Peña Olarte
Dipl. María Victoria Molina

Enero 2024
Concepción (Chile)

© 2024 Margarita León Arriagada

© 2024 Margarita León Arriagada
Se autoriza la reproducción total o parcial, con fines académicos, por cualquier medio o procedimiento, incluyendo la cita bibliográfica del documento.

ABSTRACT

Numerical methods are being implemented widely in geotechnical engineering; however, methods based on continuum mechanics are not able to provide microscale level information. Discrete Element Method (DEM) discretize the space into discrete particles and, through the analysis of micromechanical parameters that define the contact model, macroscopic behavior can be studied. DEM can capture the information at the particle level, and it has proven to be a valuable tool in the analysis of static and cyclic behavior of soils. In this study, an attempt of improving an existing calibration of the contact law parameters for Karlsruhe fine sand has been made to validate it for different testing conditions using DEM. Samples are prepared at target relative density and two types of boundary conditions are applied to explore its effect on DEM simulation. The contact law parameters for the sand are recalibrated based on the experimental results of Wichtmann and Triantafyllidis (2016). Under drained conditions, the numerical samples are able to replicate the volumetric change behavior, the dilative and contractive behavior and the initial stiffness of the experiment. The undrained behavior is examined by applying a constant volume method, where for the loose state there is a good agreement with the experimental results. Cyclic undrained results for dense samples correlates with the outcomes obtained under monotonic undrained conditions, showing a stiffer response than the experiment.

KEYWORDS: Discrete Element Method, relative density, boundary conditions, contact law, triaxial test, cyclic test.

ACKNOWLEDGMENT

First of all, I would like to thank Professor Roberto Cudmani for giving me the opportunity to work at the Zentrum Geotechnik of the Technischen Universität München and develop my thesis under the supervision of Dr. -Ing. Andrés Peña Olarte whose useful comments I thank. I must especially thank Dipl. -Ing. Maria Victoria Molina, for her patience and continuous support over the last months. Thank you for guiding me through this research with your knowledge and insightful suggestions.

My deepest gratitude goes to my beloved family, because without them none of this would have been possible. Thanks to my parents for their care and support in every choice I have made. Thanks to my siblings for their encouragement words throughout all these years, and to my nieces for being the best source of happiness I could ask for.

Lastly, this research would not have been complete without the support and motivation of my friends from all over the world. Thanks to those I met during this exchange and to those who are waiting for me back home.

Table of Contents

Index of figures

Index of tables

CHAPTER 1 INTRODUCTION

1.1 Motivation

The Discrete Element Method has gained much relevance in geomechanics since its introduction by Cundall and Strack (1979). This modeling method allows investigating the mechanical behavior of granular material under different stress conditions. Soil is considered as a collection of particles rather than a continuous medium, which makes possible to determine a realistic behavior and to have a better understanding of their physical properties.

Because of the discrete nature of granular soils, by laboratory testing it is difficult to obtain microscale information in addition to the overall macroscopic behavior of the soil. For a better understanding of macroscopic phenomena an insight into the microscopic level is required. It provides the possibility to perform localized measurements of forces at the particle contact, displacements and rotations of particles.

The triaxial test is the most often used geotechnical laboratory experiment to examine the drained and undrained behavior of soil and the continuous development of testing devices have increased the reliability of experimental testing (Bishop and Henkel, 1957). From triaxial test, the evolution of axial and volumetric strain, deviatoric stress and pore pressure can be explored, making possible to deduce fundamental properties of soil as its shear strength, cohesion, and angle of internal friction, which allows predicting the behavior in a large-scale engineering application. To understand and simulate various complex phenomena, modelling must be performed to investigate the internal mechanism of the process. Numerical simulations provide a comprehensive way to examine such complex situation (Islam, 2021).

This research work studies the macroscopic behavior of the soil from a micromechanical perspective by simulating triaxial tests using the Discrete Element Method modelling. Experimental test from the literature were replicated and compared to the obtained results.

1.2 General objetive

Comprehend the micromechanical process that occur at the particle level seeking to understand the macroscopic behavior of granular materials under monotonic and cyclic loading and drained and undrained conditions, using the DEM software YADE.

1.3 Specific objectives

1. Validate the calibrated contact model by conducting simulations of geotechnical tests under monotonic loads and undrained conditions.

2. Simulate dynamic tests with a focus on cyclic loading to evaluate liquefaction phenomena from a micromechanical perspective.

3. Provide preliminary insights on the liquefaction phenomena from micromechanical perspective.

1.4 Outline

This research work consists of five main chapters:

In Chapter 2 a literature review for topics related to this study is presented: an introduction to the Discrete Element Method and a conceptual framework on granular soils behavior under static and cyclic loading. In Chapter 3, a detailed methodology of the work was conducted, explaining the sample preparation, the generation of two types of boundary conditions, the calibration of the model parameters for Karlsruhe fine sand and how the triaxial tests were conducted. In Chapter 4, the simulations results are presented and discussed. Finally, Chapter 5 the outcomes of this research work are summarized and some recommendations for further development on this topic are mentioned.

CHAPTER 2 LITERATURE REVIEW

2.1 Discrete element method

The Discrete Element Method (DEM) is a numerical method used to describe the mechanical behavior of discontinuous materials. Introduced by Cundall (1971), the DEM was first developed for the analysis of rock mechanic problems using deformable polygonal-shaped blocks and then applied to soils (Cundall and Starck, 1979). Based on the material is made of discrete particles, this method consists in a simulation of motion, that applies contact mechanics to describe the particle interactions with its neighboring particles as shown in Figure 2.1 (B). Forces and moments act on the particles so the effect of the detected contacts can be offset, and by integration of the Newton's law of motion velocities and displacements of each particle can be computed in each step.

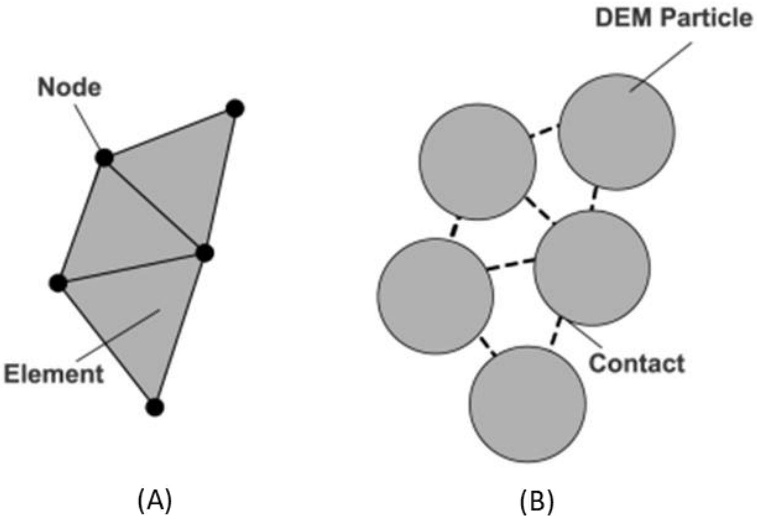

Figure 2.1: Schematic diagram illustrating (A) elements and nodes (FEM) and (B) particles and contacts (DEM) (O'Sullivan, 2004).

Different from the Finite Element Method (FEM) that divides a continuous medium to a finite number of elements that are connected by nodes (See Figure 2.1 (A)), DEM models the soil as a package of discrete particles that interact with each other in their contact zone. Numerical simulations with DEM provide more testing options and useful results than laboratory tests, due to the micromechanical response of the physical material (deformability, strength, dilatancy, strain location and others) can be reproduced by determining the micro-properties of the material as normal, tangential and rolling stiffness and local friction (Belheine et al., 2009). In addition, DEM allows finite displacements and rotations of discrete bodies, including complete detachment, and while the calculation progresses, recognizes new contacts automatically.

The basic features that define the Discrete Element Method are:

- Particles are discrete elements that together comprise a complex system of particles.
- These discrete elements move independently and interact with each other in the contact zones.
- At particle level, rigid body mechanics are used, and the discrete elements are considered rigid elements.

On the other hand, although it is a valuable tool, this method has computational limitations, as the model resolution at particle scale is computationally expensive and it is limited to the computational power.

A typical DEM simulation starts with the creation and spatial orientation of the particles, which can be represented as spheres, polyhedral, among others. As the particles interact at contacts according to simple physical laws, and a finite difference (time-stepping) algorithm is applied, the software detects in each iteration the total amount of contacts between particles through collision detection engines. The forces and moments between particles resulting from the contact impel the particles into new positions within each time step by solving Newton’s equation of motion. The acceleration is determined by the Newton’s second law, then is integrated one time for obtaining the velocities, and then one more time for the displacements used to determine the new positions of the particles.

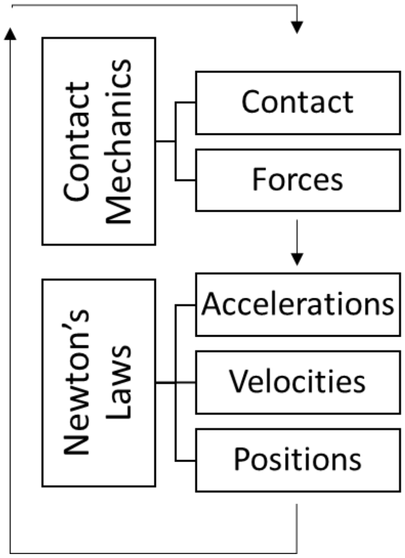

Figure 2.2: Flowchart of simulation for particle behavior using DEM.

2.1.1 Kinematic variables

In this section two spheres with initial centers at $\overrightarrow{C_1}$ and $\overrightarrow{C_2}$ and radius r_1 and r_2 as presented in Figure 2.3 are considered.

2.1.1.1.Normal displacement

As two particles come into contact, an overlap occurs at the central part of the contact until equilibrium is reached. This equilibrium position is represented by the equilibrium distance d_0, measured from the centers of the spheres, where neither repulsive nor attractive forces act on both spheres (Equation 2.1). The overlap distance u_n is used to determine the normal forces based on the normal stiffness and is calculated as follows:

$$d_0 = \left|\overrightarrow{C_2} - \overrightarrow{C_1}\right| \tag{2.1}$$

$$u_n = r_1 + r_2 - d_0 \tag{2.2}$$

Where,

$\overrightarrow{C_{1,2}}$ = Position vectors of the spheres

$r_{1,2}$ = Spheres radius

d_0 = Equilibrium distance

u_n = Overlap distance or normal displacement

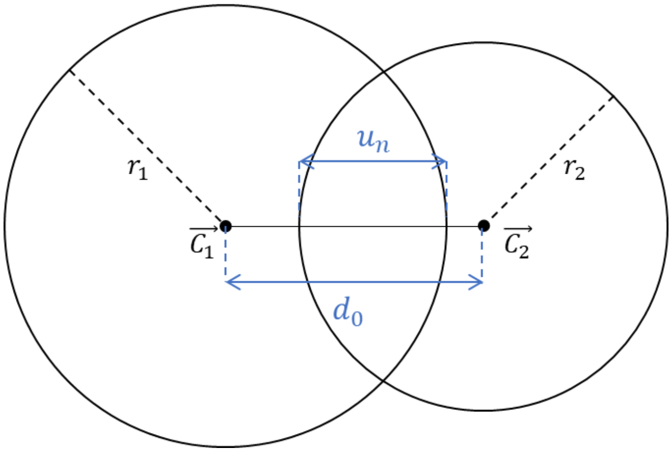

Figure 2.3: Overlap of particles u_n used to compute the normal forces.

2.1.1.2.Shear displacement

The shear displacement u_t is perpendicular to the contact plane along the n axis (Figure 2.4). For the calculation of the tangential force component, both linear and rotational relative movement are taken into account. To obtain the shear displacement, the tangential velocity v_t at the contact point must be determined by:

$$v_t = v_r - (v_r \cdot \vec{N})\vec{N} \tag{2.3}$$

Where,

v_r = Relative velocity between particles

$\vec{N}$ = Unit normal vector

$$v_r = \left(\dot{u}_2 + \omega_2 \times \overrightarrow{C_2}\right) - \left(\dot{u}_1 + \omega_1 \times \overrightarrow{C_1}\right) \tag{2.4}$$

Where,

$\dot{u}_{1,2}$ = Translational velocity of both spheres

$\dot{\omega}_{1,2}$ = Rotational velocity of both spheres

$\overrightarrow{C_{1,2}}$ = Position vectors of the spheres

$$u_t = v_t \Delta t \tag{2.5}$$

Where,

u_t = Shear displacement

v_t = Tangential velocity

Δt = Time step

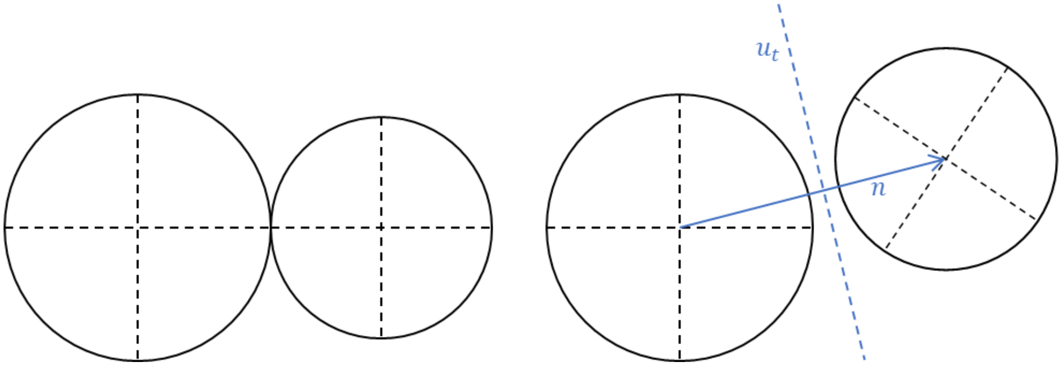

Figure 2.4: Shear displacement u_t.

2.1.2 Contact laws

In simulations, the mechanical behavior of the material is defined by the application of constitutive models in DEM, also known as contact laws that will compute the contact forces existing between particles using the kinematic variables previously defined.

This model resolves the contact force between two perfectly elastic spheres into normal and shear components with respect to the contact plane:

$$\vec{\boldsymbol{F}} = \overrightarrow{\boldsymbol{F_n}} + \overrightarrow{\boldsymbol{F_s}} \tag{2.6}$$

Where,

$\vec{F}$ = Contact force

$\overrightarrow{F_n}$= Normal component of the contact force

$\overrightarrow{F_s}$= Shear component of the contact force

The normal contact force is calculated from the overlap distance of the particles in contact:

$$\overrightarrow{F_n} = k_n u_n \vec{N} \tag{2.7}$$

Where,

k_n = Normal stiffness at the contact

u_n = Overlap distance or normal displacement

$\vec{N}$ = Unit normal vector

The normal stiffness can be calculated as follow:

$$k_n = E_c \frac{2r_1 r_2}{r_1 + r_2} \tag{2.8}$$

Where,

E_c = Contact stiffness

$r_{1,2}$ = Spheres radius

In the other hand, the shear contact force is calculated by:

$$\overrightarrow{F_s} = k_t u_t \tag{2.9}$$

Where,

k_t = Shear stiffness

u_t = Shear displacement

The shear stiffness k_s is calculated as follow:

$$k_s = E_c v_c \frac{2r_1 r_2}{r_1 + r_2} \tag{2.10}$$

Where,

v_c = Contact stiffness ratio

Is important to explain the difference between the contact stiffness E_c and the Young's Modulus E, since the first one characterizes the contact at the particle scale and tends to be larger than the Young's Modulus, that is directly related to the material at the macro scale.

Moreover, a limiting value for the shear force is established, based on the Mohr-Coulomb equation, and implemented to check whether sliding will occur at the contact of grains.

$$\overrightarrow{F_s} \leq \overrightarrow{F_n}\tan(\varphi) \tag{2.11}$$

Where,

φ = Contact friction angle

Particles in DEM can have different geometries, but in order to keep a low calculation cost, usually the spherical particle shape is chosen (Widulinski, 2009). It is shown that spherical particles have a smaller angle of repose and reduced shear strength as compared to non-spherical particles (Rothenburg and Bathurst, 1992), which is why to simulate the effect of particle non-spherical shape and grain roughness, contact moments were introduced into the model increasing the rolling resistance. The contact moment increments are calculated based on the rotational stiffness k_r calculated as:

$$k_r = \beta k_t r_1 r_2 \tag{2.12}$$

Where,

β = Dimensionless rotational stiffness coefficient

The contact moment increment is calculated based on the rotational stiffness as:

$$\Delta M = k_r \Delta\vec{\omega} \tag{2.13}$$

Finally, the rotational moment $\vec{M}$ is limited by the rotational coefficient η:

$$\vec{M} \leq \eta \frac{r_1 + r_2}{2}\overrightarrow{F_n} \tag{2.14}$$

Where,

$\overrightarrow{F_n}$ = Normal contact force

η = Rotational coefficient

The contact law ‘Linear elastic with simple friction and simple rotation’ is used for the purposes of this study and is described in the following section.

2.1.2.1.Linear elastic with simple friction and simple rotation

It is comprised of two parts: One related to the simple friction and the other related to simple rotation. The first one can be identified as a whole law called ‘Linear elastic with simple friction’ that was defined by Cundall and Strack (1979) and requires four contact parameters. This law is for linear compression and Mohr-Coulomb plasticity surface without cohesion.

The second part of the law was introduced as a modification of the previous linear elastic and perfectly plastic law by Iwashita and Oda (1998). It requires six contact parameters in total, because a rotational component is added along with the tangential component, which will be detailed below.

1. Contact stiffness E_c
2. Contact stiffness ratio $v_c = k_n/k_s$
3. Contact friction angle φ
4. Material density ρ
5. Rotational stiffness k_r
6. Rotational coefficient η

Because this contact model is an extended variant of the ‘Linear elastic with simple friction contact’ law, there is a provision of ‘switches’ for the command that applies the contact law ‘*CohFricMat’* that create the law in YADE, which is used to switch rotation or cohesion off. When the rotation component is switched off, it behaves as the original law, otherwise it behaves as a linear elastic with simple friction and simple rotation, as predicted. The response of normal and tangential contact models is shown in Figure 2.5.

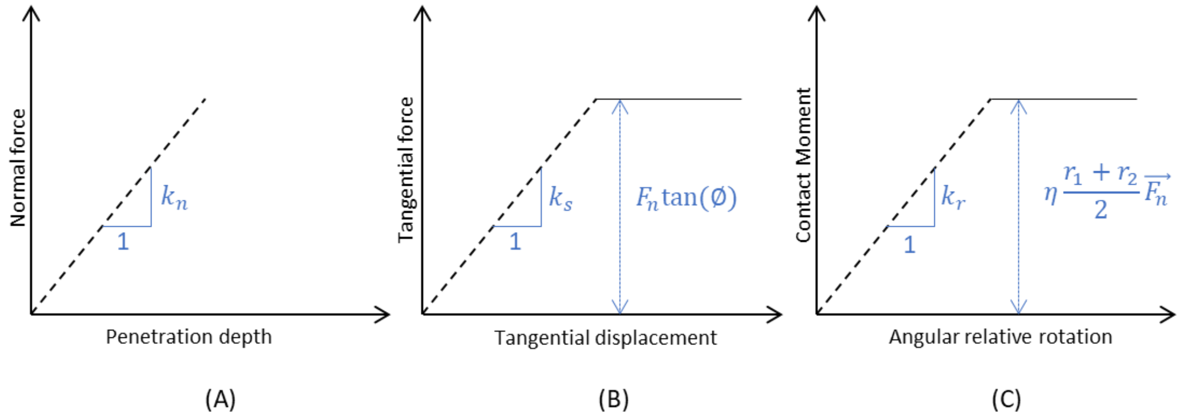

Figure 2.5: Mechanical response of the (A) normal contact model, (B) tangential contact model and (C) rotational contact model (Basson et al., 2010).

2.1.3 Stability considerations

2.1.3.1.Numerical damping

In order to keep numerical stability of the simulations and to reach a quick convergence of the unbalanced forces to a quasi-static balance state of the group of particles, the kinetic energy must be dissipated by introducing numerical damping. As contact laws does not include damping based on velocity, an artificial numerical damping can be introduced by decreasing forces which increase the particle velocities and vice versa, comparing the current acceleration sense and particle velocity sense. This is done by component, which makes the damping scheme clearly non-physical, as it is not invariant with respect to coordinate system rotation; on the other hand, it is very easy to compute (Šmilauer, 2021).

YADE provides the function '*NewtonIntegrator*', where damping coefficient is specified as '*NewtonIntegrator.damping*'. This function affects all the particles in the same way, despite their own frequencies.

2.1.3.2.Critical timestep

The discrete element method uses an explicit scheme of numerical integration to solve the equations of motion; however, this is only conditionally stable. The stability condition is given by time interval between two successive functions execution Δt, for what is useful to stablish a limit value for the time step called critical time step Δt_{cr}. Δt_{cr} depends on the particle properties as the quantity of particles, number of contacts, stiffness and contact density (O'Sullivan, 2004). Finally, to secure the stability of the method the time step must be lower than the critical timestep.

$$\Delta t \leq \Delta t_{cr} \tag{2.15}$$

The critical timestep is calculated as:

$$\Delta t_{cr} = \frac{2}{\omega_{max}} \tag{2.16}$$

Where,

ω_i = Higher natural frequency inside the system

The natural frequency for each element on the system is:

$$\omega_i = 2\sqrt{\frac{k_i}{m_i}} \tag{2.17}$$

Where,

k_i = Particle stiffness

m_i = Particle mass

To define the time step of the simulation, YADE provides functions such as '*GlobalStiffnessTimeStepper*', which calculates it based on the particle stiffness for each contact (k_i, k_j), varying Δt in each iteration, due to the contact number changes along the simulation.It supposes each contact has normal stiffness, shear stiffness and it is oriented by the contact plane normal (Šmilauer, 2021).

When no contacts occur between particles the critical time step $\Delta t_{cr} = \infty$, since $\omega_{max} = 0$. In this case the time step estimation is based on the wave propagation velocity v_{wave} (See Equation 2-18), which shall not propagate further than a minimum distance $d_{min} = r_i$. Considering the Equation 2-19, is noticeable that higher contact stiffness will make the timestep decrease and resulting in decreasing the particle displacement during the timestep, which in case of model rigid particles will lead to high calculation times. To conclude, the contact stiffness is an important parameter to consider when obtaining accurate results within a reasonable simulation time.

$$v_{wave} = \sqrt{\frac{E_c}{\rho}} \tag{2.18}$$

$$\Delta t_{cr} = r_i \sqrt{\frac{\rho_i}{E_i}} \tag{2.19}$$

Where,

r_i = Particles radius

ρ_i = Particle density

E_i = Particle contact stiffness

This time step calculation is implemented in YADE by means of the ‘*utils.PWaveTimeStep*’ function. It shows significant overestimation on the critical time step since it considers a certain amount of number of contacts per particle and makes simplifying assumptions: the function takes a ‘reasonable’ contact number given the radius distribution. To guarantee a stable simulation, the developers of the software YADE recommend using a percentage of the critical timestep given by the *PWaveTimeStep* algorithm $\Delta t = 0.3\Delta t_{cr}^{Pwave}$ (Šmilauer, 2021).

2.1.4 Fabric parameters

In micromechanics, soil ‘fabric’ is an all-encompassing term used to describe the arrangement of particles, particle groups and void spaces etc. in the soil (Mitchell and Soga, 2005). The microstructure of granular assemblage can be manifested by a variety of fabric indices, such as the number of contacts and voids (Wang and Wei, 2016).

2.1.4.1.Coordination number

It is the average number of interactions that particles have with neighboring particles. YADE provides a function called ‘*avgNumInteractions()*’ which returns the average number of contacts per particle or coordination number Z, by means of the following equation:

$$Z = \frac{2C}{N} \tag{2.20}$$

Where,

C = Total number of contacts within the arrange of particles

N = Total number of particles

Activating the 'skipFree' switch in the function, particles not contributing to stable state of the packing are skipped. The mechanical coordination number Z_m is then estimated following the equation given by Thornton (2000):

$$Z_m = \frac{2C - N_1}{N - N_1 - N_0} \tag{2.21}$$

Where,

N_1 = Number of particles with only one contact

N_0 = Number of particles with no contacts

Coordination number is influenced by the presence of walls surrounding the package, as in this area there is less contact between particles, creating bigger void spaces than in the rest of the sample. This effect is observed in a range area up to 1-2 sphere mean diameter from the wall. The '*avgNumInteractions()*' function has a 'cutoff' parameter which can help to reduce the wall effects by excluding this area of the sample's bounding box from the calculations.

2.1.4.2.Void ratio

In YADE the '*voxelporosity()*' function calculates the porosity by dividing the volume into a dense grid of cubes or voxels, defining the porosity n as:

$$n = \frac{V - V_v}{V} \tag{2.22}$$

Where,

V = Sample volume

V_v = Volume of voxels that fall inside the sphere

Then, the void ratio e can be calculated by:

$$n = \frac{e}{1 + e} \tag{2.23}$$

Where,

n = Porosity

One of the most important parameters for porosity calculation is the size/resolution of the cubes. High-resolution values throw better accurate results but increase the computation time. This function is also used to calculate the porosity in any sub-volume defined within the sample volume allowing studying and reducing the wall effects.

2.1.5 Inertial number

According to Modenese et al. (2012), it must be ensured that numerical simulations run under quasi-static conditions to compare the experimental and numerical results, avoiding the influence id dynamic effects. For a sample to be considered under quasi-static conditions, the stress-strain-volume change behavior must be rate-independent. To define the quasi-static state, a dimensionless parameter called inertial number I is used (Da Cruz et al., 2005):

$$I = \dot{\varepsilon} d \sqrt{\frac{\rho}{\sigma'}} \tag{2.24}$$

Where,

$\dot{\varepsilon}$ = Strain rate

ρ = Density of the material

σ' = Mean effective stress

d = Mean particle size

Using small values of strain rate results on small values of I which corresponds with the quasi-static condition: $I \leq 10^{-2}$ (Da Cruz et al., 2005). The inertial number should be chosen in such a manner that the inertia forces are smaller than the contact forces to maintain the quasi-static condition (Cundall and Strack, 1979) and according to the results obtained by Lopera Perez et al. (2016), low inertial number shows a highly dilative behavior.

In quasi-static regime, the effect of inertial forces is insignificant, and the simulation under quasi-static conditions are independent of strain rate. Lopera Perez et al. (2016) found reliable simulation results were obtained when the value for the inertial number is less or equal to $2.5e^{-3}$.

2.2 Granular soil behavior under static loading

2.2.1 Shear strength of soil

It can be defined as the ultimate or maximum shear stress the soil can withstand (Holtz and Kovacs, 1981). The parameters that characterize the shear strength of soils are determined by several laboratory shear tests, but the most common one is the triaxial test.

To represent the soil stress-strain behavior and the volumetric variation-strain behavior under triaxial compression, the deviatoric stress q is calculated as:

$$q = \sigma'_1 - \sigma'_3 \tag{2.25}$$

Where,

σ'_1 = Effective major principal stress

σ'_3 = Effective minor principal stress

Under drained conditions the effective stresses are used, so the deviatoric stress is defined as $q = \sigma_1 - \sigma_3$. Figure 2.6 shows the stress-axial strain and the volumetric strain-axial strain response of granular soils under drained triaxial compression.

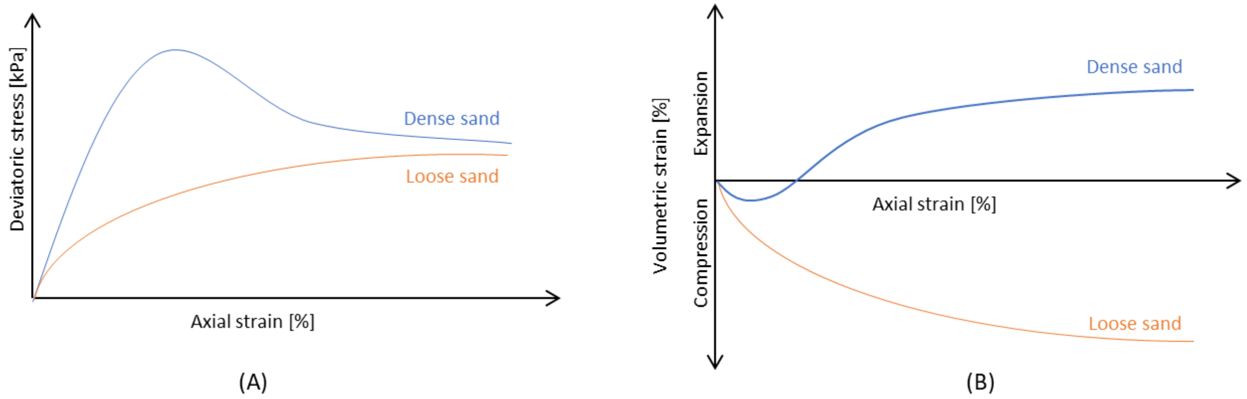

Figure 2.6: Granular soil (A) stress-strain behavior and (B) volumetric behavior for dense and loose samples.

At large axial strains the ultimate shear stress is achieved asymptotically for both the dense and the loose sample, regardless the initial void ratio. In the same Figure 2.6, it can be observed that for samples prepared with the same confining pressure, loose material tends to lose volume, meaning that is compressed and dense material lose volume initially so then it starts to increase the volume, having a dilatating behavior.

2.2.2 Critical state

The critical state has been defined as the state at which the soil deforms continuously at constant void ratio and constant stress (Zhao and Evans, 2011). This final void ratio was called critical void ratio and proved to be dependent of the initial confining effective stress (Taylor, 1948).

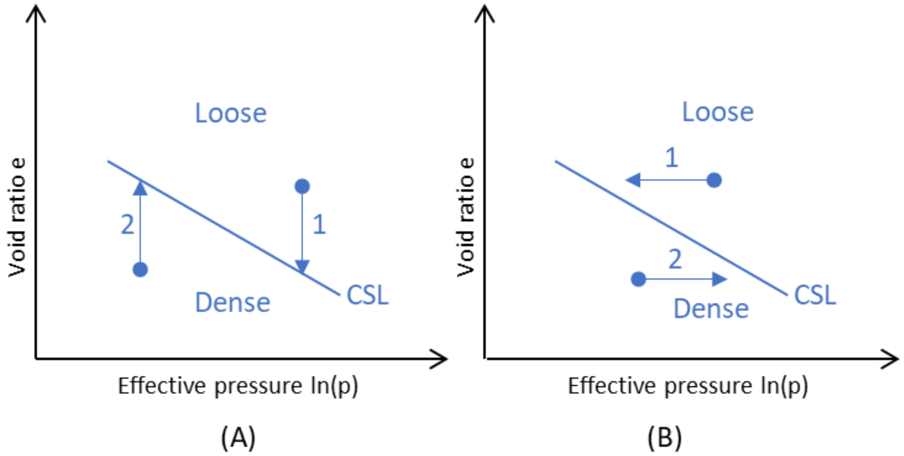

Figure 2.7: Critical state line and volumetric response for soils under (A) drained conditions and (B) undrained conditions.

The critical state line (CSL) represents the correlation between the critical void ratio e_{cs} and the effective mean stress p' (Equation 2.26). This line enables to classify different types of soils: The soil samples that initial conditions located it above the CSL, will be denominated as loose, meanwhile the samples located under the CSL will be denominated as dense.

$$p' = \frac{\sigma_1 + \sigma_2 + \sigma_3}{3} \tag{2.26}$$

Granular soil behavior can be described based on the correlation between the initial void ratio and the critical void ratio by means of the state parameter ψ (Been and Jefferies, 1985), used to characterize the volumetric response of the soil. $\psi < 0$ corresponds to dilatant behavior, and $\psi > 0$ corresponds to contractive behavior.

$$\psi = e_0 - e_{cs} \tag{2.27}$$

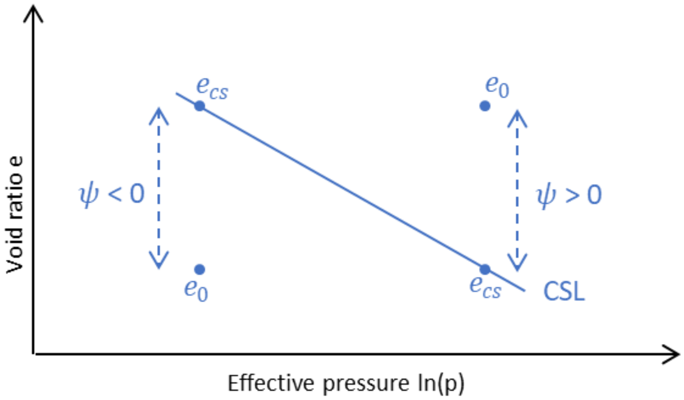

Figure 2.8: State parameter ψ.

2.2.3 Steady state in undrained triaxial test

The steady state line (SSL) represents the presence of a unique line in the plot of void ratio against the effective mean principal stress at which the sand undergoes large deformation under constant void ratio, effective confining stress and shear stress. There is also another unique line termed as a quasi-steady state line (QSSL) which represents the combination of the void ratio e and the effective mean principal stress p' at which the minimum shear strength is mobilized at medium to large shear strain (Tsukamoto and Ishihara, 2022). When the void ratio is significantly large, the steady state line and quasi-steady state line become coincident. At a medium to greater density, the quasi-steady state occurs at lower effective confining stress than steady state, leaving the QSSL always located at a lower position than the SSL in the e - p' plot (Figure 2.9).

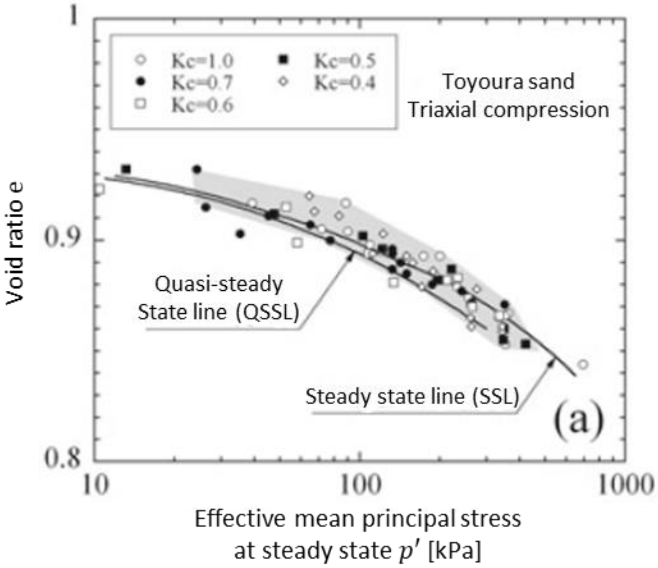

Figure 2.9: Steady state lines in triaxial compression for Toyoura sand void ratio against effective mean principal stress (Tsukamoto and Ishihara, 2022).

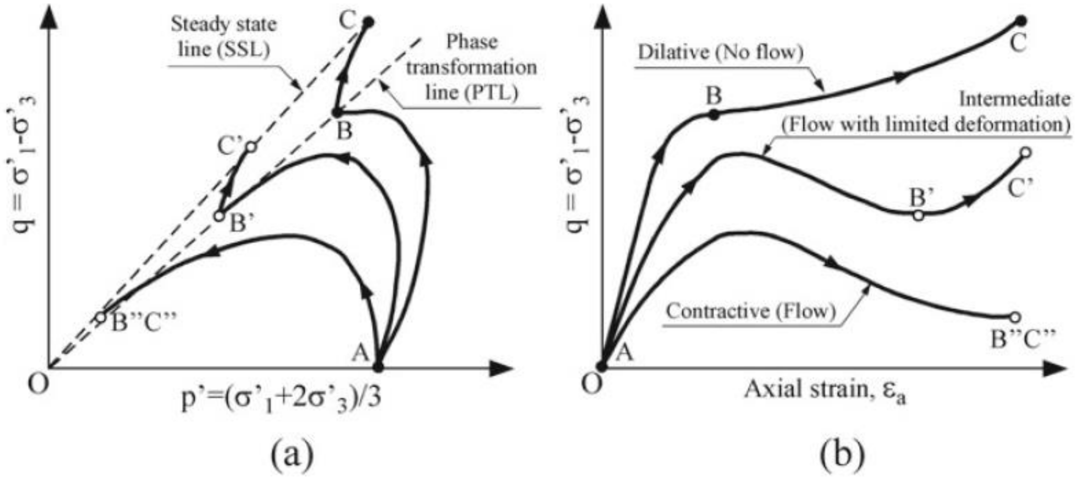

Figure 2.10: Schematic diagram showing typical behavior during the isotropically consolidated undrained compression (a) effective stress paths (b) stress-strain relations (Tsukamoto and Ishihara, 2022).

As shown in Figure 2.10, the point A indicates that the specimens are isotropically consolidated with a given effective confining stress. The different kinds of undrained behavior depend on the density of soil specimens: The dense sample shows dilative behavior along the state of phase transformation B and the steady state C. The medium dense sample shows intermediate behavior along the quasi-steady state B' and the steady state C'. The loose sample shows contractive behavior along the quasi-steady state B'' and the steady state C'', where points B'' and C'' coincide.

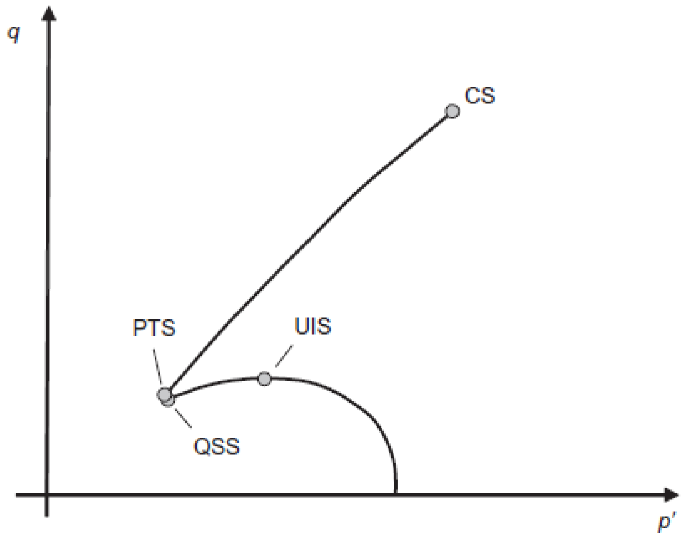

Figure 2.11: Characteristic state of undrained shearing behavior of sands: critical state (CS), phase transformation state (PTS), quasi-steady state (QSS) and undrained instability state (UIS) (Murphy, 2007).

Experimental results show that the QSS constitutes a distinct soil state, which, strictly speaking, does not coincide with the PT. Nonetheless, the shear at the QSS and PT are almost identical (Murphy, 2007).

Figure 2.11 shows the instability state, at which the deviatoric stress q reaches a local and temporary maximum.

2.3 Granular soil behavior under cyclic loading: Liquefaction phenomena

According to Sladen (1985), liquefaction can be defined as a: "Phenomenon wherein a mass of soil loses a large percentage of its shear resistance, when subjected to static, cyclic, or shock loading, and flows in a manner reassembling a liquid until the shear stresses acting on the mass are as low as the reduced shear resistance".

The load application method can be classified into three types: Slow static loading, rapid or transient loading and cyclic loading, as illustrated in Figure 2.12. In the first one, the load is applied monotonically. In case the loading to failure is executed in a shorter time than the monotonic loading, is called rapid or transient loading. The term cyclic loading test will be used to imply the test in which rapid loads are repetitively applied (Ishihara, 1996).

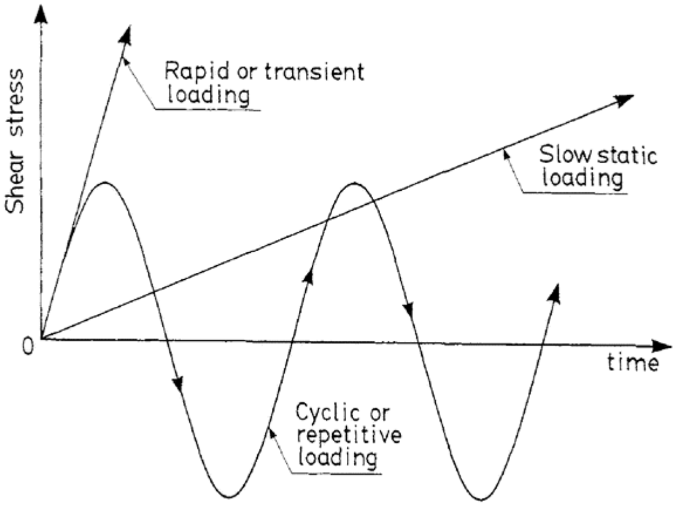

Figure 2.12: Types of loading (Ishihara, 1996).

Relevant soil parameters in the liquefaction behavior that determine the susceptibility of occurrence are the particle size distribution and the relative density because cyclic behavior is governed largely by the looseness or denseness of the material (Tsukamoto and Ishihara, 2022). The fraction of fines and the plasticity indices are factors that also affect directly in the material behavior, although, according to Seed et al. (2003), plasticity is more relevant as a susceptibility criterion.

2.3.1 Particle size distribution

To determine the percentage of diverse grain sizes that compose the soil, a laboratory sieve analysis for coarse particles of sand and laboratory sedimentation analysis for fine particle of silt and clay are needed. This soil classification is useful to estimate soil properties as permeability and strength.

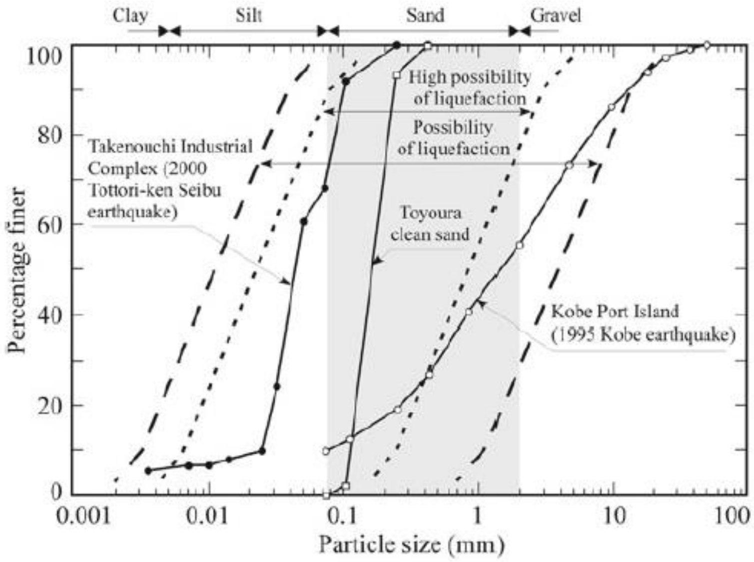

Figure 2.13: Particle size of soil pertinent to soil liquefaction triggering (Tsukamoto and Ishihara, 2022).

As Figure 2.13 shows, the particles in the range of 0.08-2 mm fall into the sand fraction, the range where there is a high possibility of liquefaction occurrence. The Karlsruhe fine sand mean particle size is 0.14 mm.

2.3.2 Cyclic mobility

Defined by Casagrande (1976) as the progressive softening of a saturated sad specimen when subjected to cyclic loading at constant water content.

Figure 2.14 (A) shows the plot of stress path, in terms of the deviator stress q against the effective mean stress p', where q is defined by Equation 2-25 and $p'$by Equation 2-26. After isotropic consolidation, the stresses have the values of $\sigma_1 = \sigma_3 = \sigma'_o$, where σ'_o represents the initial effective confining stress. For this example, the effective mean stress p' begins to reduce from σ'_o=100 kPa, while the stress cycles application continues the excess pore water pressure increases. When the effective stress becomes equal to zero, and the stress point tends to move along the failure envelope.

In subsequent stress cycles, the effective mean stress tends to recover as the stress deviator amplitude increases, creating a butterfly-like loops close to the origin of the p' - q plot.

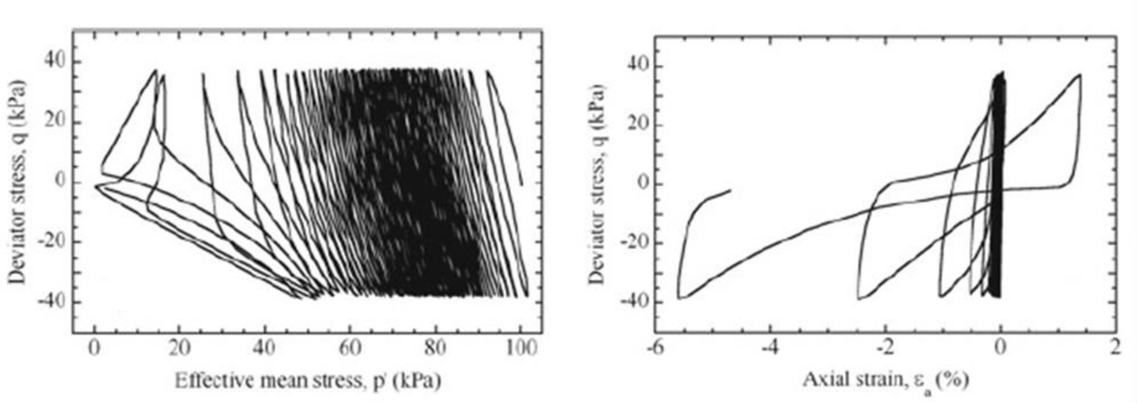

(A) (B)

Figure 2.14: Plots of (A) effective stress path p'-q and (B) axial strain ε_a - deviatoric stress q curves for Tohoku cilica sand Dr=60% (Tsukamoto and Ishihara, 2022).

The plots q - ε_a are shown in Figure 2.14 (B), where the curves exhibit rather stiff response initially, increasing rapidly the axial strain ε_a towards extension as the cyclic stress application is continued. This rapid increase if axial stain is associated with the development of excess pore water pressure.

2.4 Conclusions

An enlightenment of the Discrete Element Method was presented in the first part of the chapter, describing the kinematic variables, the selected contact law, the importance of reaching the stability conditions considering the fabric parameters during the granular assemblage and their impact on the soil behavior.

The second and third part of the chapter concentrates on granular soils behavior under static and cyclic loading, specifically addressing triaxial tests expected behavior and providing a foundation for understanding the dynamic response of granular soils.

CHAPTER 3 METHODOLOGY

3.1 Introduction

This chapter outlines the methodology employed for conducting the modeling process. It explains each step of the sample preparation and the configuration of the software taking into account the type of boundary and the drainage conditions under the triaxial tests were executed, besides considering the loading conditions.

3.2 Sample preparation

3.2.1 Testing material

The material under study for the development of this thesis is the ‘Karlsruhe fine sand’. The results of the experimental database compiled by Wichtmann and Triantafyllidis (2016) are taken as a reference. The tested material shown in Figure 3.1 has almost no fines content, a predominantly subangular shape of the grains, a mean grain size $d_{50} = 0.14$ mm and a uniformity coefficient $C_u = 1.5$. The minimum and maximum void ratios $e_{min} = 0.677$ and $e_{max} = 1.054$ were determined from standard tests (at mean pressure $p = 0$) according to DIN 18126. The sand properties are summarized in Table 3.1.

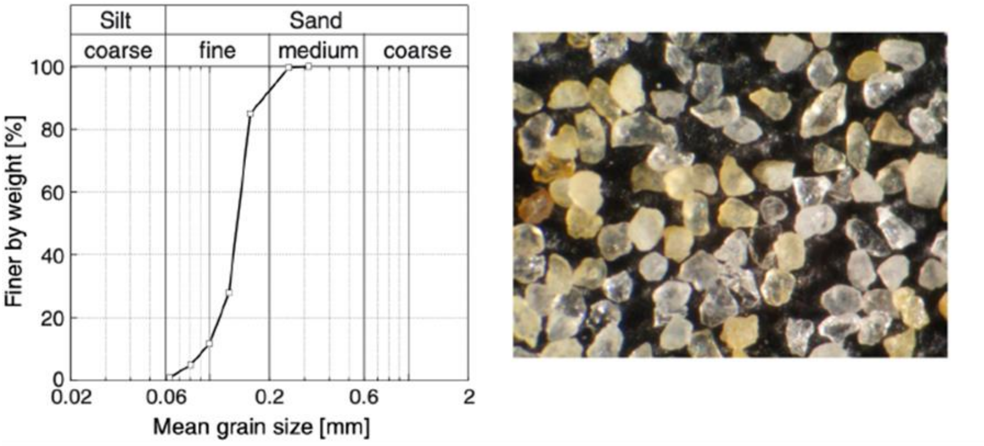

(A) (B)

Figure 3.1: Karlruhe fine sand (A) tested grain size distribution curve and (B) microscopic view of the grains (Wichtmann and Triantafyllidis, 2016)

Table 3.1: Properties of Karlsruhe fine sand (Wichtmann and Triantafyllidis, 2016)

Grain shape	**d_{50} [mm]**	**$C_u = \frac{d_{60}}{d_{10}}$ [-]**	**e_{min} [-]**	**e_{max} [-]**
Sub-angular	0.14	1.5	0.677	1.054

3.2.2 Boundary generation: Rigid boundaries

These boundaries are rigid planes defined by three-point coordinates also called ‘walls’, which collide with the particles enclosed by them. No particle can cross this boundary; instead, the particle bounces back inside the border. Similar to particles, material properties and governing contact law must be defined for the boundaries. In YADE the friction can be assigned to the by specifying a friction angle for the wall’s material.

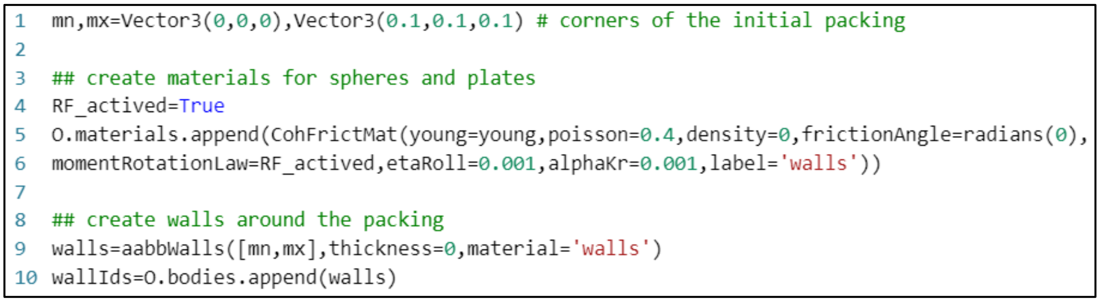

```
1  mn,mx=Vector3(0,0,0),Vector3(0.1,0.1,0.1) # corners of the initial packing
2
3  ## create materials for spheres and plates
4  RF_actived=True
5  O.materials.append(CohFrictMat(young=young,poisson=0.4,density=0,frictionAngle=radians(0),
6  momentRotationLaw=RF_actived,etaRoll=0.001,alphaKr=0.001,label='walls'))
7
8  ## create walls around the packing
9  walls=aabbWalls([mn,mx],thickness=0,material='walls')
10 wallIds=O.bodies.append(walls)
```

Line 5 of the shown code creates the material for the walls, where ‘*CohFricMat*’ is the selected contact law which was explained in the previous chapter. Hence, the parameters to be defined are the contact stiffness E_c, contact stiffness ratio v_c, contact friction angle φ, density ρ, rotational stiffness k_r and rotational coefficient η. Line 9 creates an axis-aligned bounding box, according to the given extreme corners coordinates of the package given in Line 1.

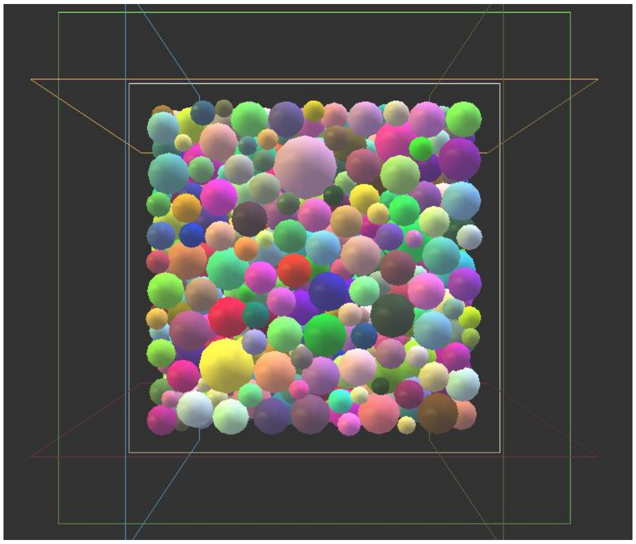

Figure 3.2: Rigid boundaries on all sides of a cubical space.

3.2.3 Boundary generation: Rigid boundaries

When utilized, particles can cross this type of boundary without resistance and new particles automatically reappear in the same position and with the same initial translational and angular velocity on the opposite side of the simulation border. These boundary conditions are applied to understand the granular material behavior in uniform strain field and to remove the boundary effects, since in samples with rigid boundaries a higher void ratio is obtained. This can be visualized by considering the void ratio variation across layers before and after the loading application: the void ratios of the boundary layers in the specimen with rigid walls are larger than those of the layers in the middle (Zhang, 2018).

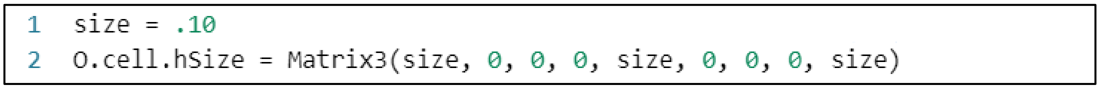

```
1  size = .10
2  O.cell.hSize = Matrix3(size, 0, 0, 0, size, 0, 0, 0, size)
```

Contrary to the rigid boundaries case, the code does not define a material for the boundaries, however Line 2 of the code above defines the size of the cell where the spheres are to be contained.

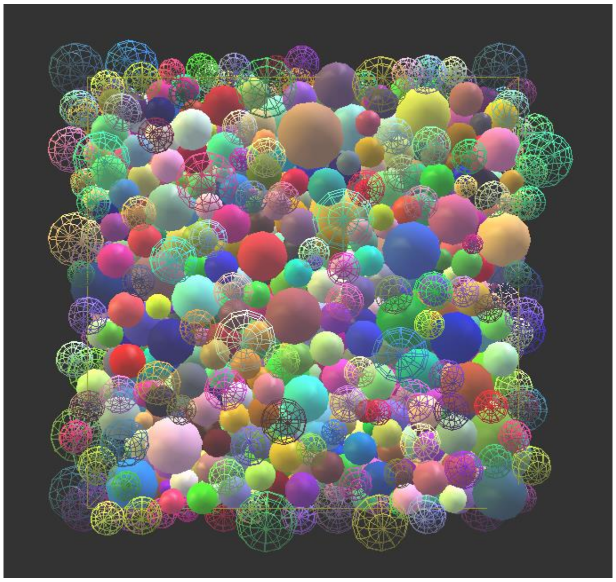

Figure 3.3: Periodic boundaries on all sides on a cubical space.

3.2.4 Maximum and minimum void ratio

Isotropic compression is the method used to prepare the samples and determine the maximum and minimum void ratio in DEM. Defining a low contact friction angle value during the compression phase allows to obtain the densest soil state and defining a high contact friction angle to reach the loosest soil state.

The friction angle was set to 0° and 27° (friction coefficient 0 and 0.51), obtaining the densest and loosest sample respectively. Also, friction angle of 18° (friction coefficient 0.34) is considered as the critical friction angle. The initial confining pressure is 100 kPa, meaning that the maximum and minimum void ratios are to be determined under that confining condition.

Knowledge of these values is important to determine the relative density of the specimens during the sample preparation phase.

3.2.5 Compression curves

In order to study the confining pressure dependence of the void ratio values, the samples where further compressed until reaching a confining pressure of 400 kPa. The variation of the limiting void ratios

e_{max} and e_{min} against mean pressure p is plotted. The upper limit curve must be adjusted due to the curve poses a destabilization at the beginning, as Figure 3.4 shows. The reason of this behavior is that linear contact law works effectively until the critical friction angle of soil, beyond the dilation control the behavior which is not modelled in the isotropic compression simulation (Basson, 2018). The maximum void ratio will be determined as the initial value of the 'fixed' curve. There is no need to adjust the lower limit curve because it does not present any destabilization, meaning that the minimum void ratio will be the first value of that curve.

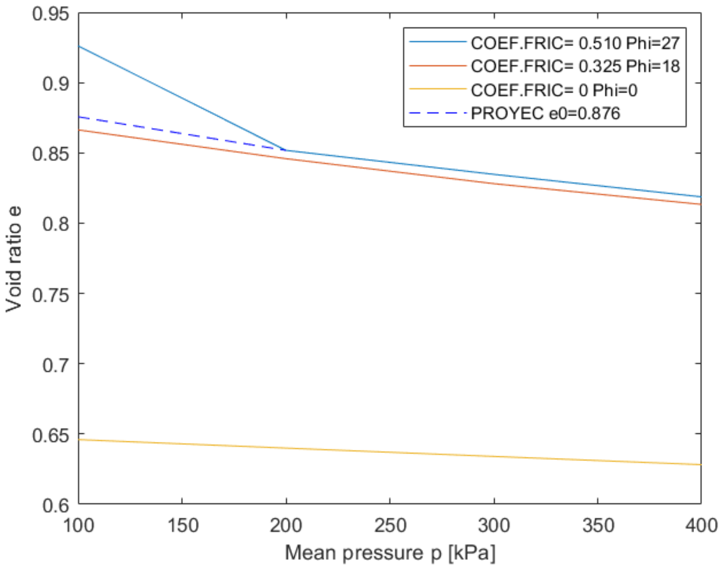

Figure 3.4: Compression curves and limiting void ratios determination.

3.2.6 Sample preparation at target relative density

Since the subangular sand grains are represented in DEM with spheres for simplification, it is not likely to reproduce the void ratio values of the experimental samples, which are higher for a given relative density. Therefore, in order to create numerical samples that are comparable to the experimental ones, samples are prepared with the same the relative density RD instead of with the same void ratio.

$$RD = \frac{e_{max} - e_0}{e_{max} - e_{min}} \tag{3.1}$$

Where,

e_{max}= Maximum void ratio

e_{min} = Minimum void ratio

e_0 = Initial void ratio of the sample at that relative density

For the sample a cloud of 1000 spherical particles is created to avoid high computational times. The specimens are then subjected to isotropic compression at a given confining pressure according to the experimental samples. Samples with different relative density are prepared varying the friction angle degree during isotropic compression. In YADE there are two methods to reach the desired confining pressure: controlling the velocity that the walls move inwards with keeping the particle size constant or increasing the volume of the particles until they occupy the box space and exert the pressure on the walls. When they reach the defined confining pressure inside the bounding box, the sample is preparation is finished.

Once the samples are prepared at a given confining pressure, the relative density of each one is determined by means of the Equation 3.1.

3.3 Triaxial tests

The triaxial test is one of the most reliable existent methods to determine the shear strength parameters. The reasons why this method is widely used in research are that it provides information about the stress-strain behavior of the soil that the direct shear test does not, as pore pressure changes and the fact that the state of stress at all intermediate stages upto failure is known. It also provides more uniform stress conditions than the direct shear test by concentrating the stress along the plane of failure, and it provides more flexibility in terms of loading path (Braja, 2001).

3.3.1 Monotonic drained triaxial test

In YADE, the loading conditions for the triaxial test on samples with rigid boundaries are applied by the engine '*TriaxStressController*', which maintain constant stresses or constant strain rates on selected walls of a paralepidid packing with rigid boundaries. The stress/strain control is defined for each axis using the command *'stressMask'* and target values are defined by goal1, goal2, and goal3 (Šmilauer, 2021).

During the confining phase, the bitmask '*TriaxStressController.stressMask'* must be defined, which determines whether the imposed goal values are stresses or strain rates. As the value is 7, three of the goal values are stresses exactly as Line 5 shows. The confining pressure that will be applied is defined in Line 4 of the given code below.

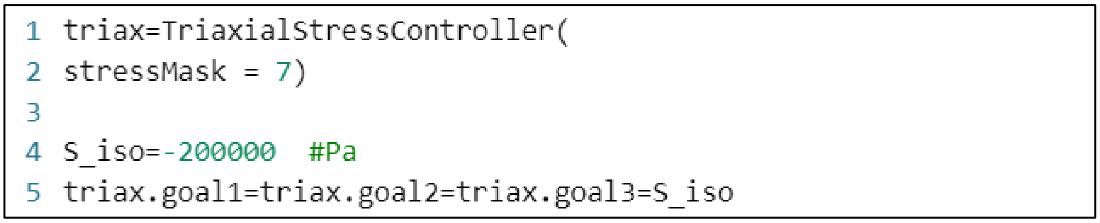

```
1  triax=TriaxialStressController(
2  stressMask = 7)
3
4  S_iso=-200000  #Pa
5  triax.goal1=triax.goal2=triax.goal3=S_iso
```

For the deviatoric loading phase, in Line 10 of the code below, the bitmask '*TriaxStressController.stressMask'* is set to 5, meaning that two of the goal values will be stresses, which is verify in Lines 13 and 14. Line 18 shows that once the defined axial strain goal is achieved, the simulation is terminated.

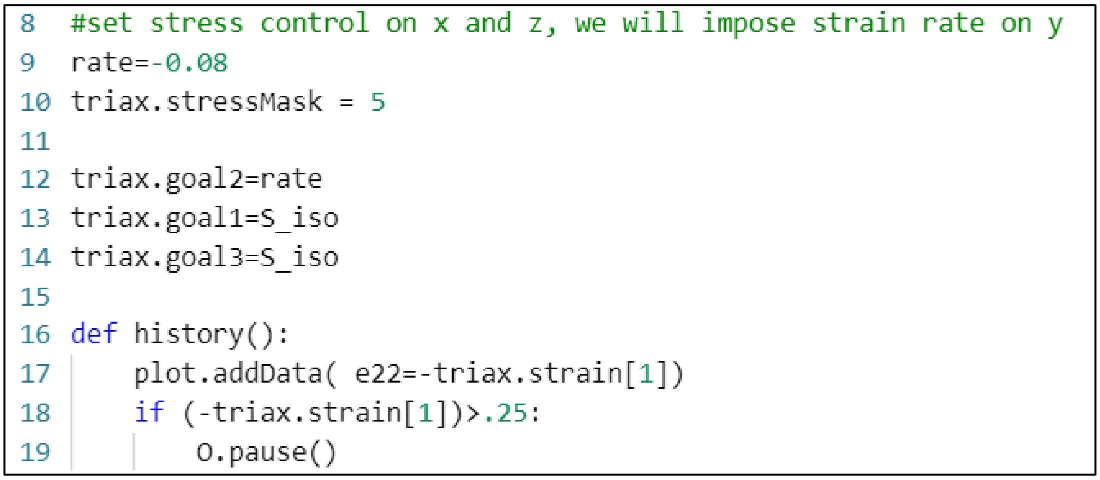

```
8  #set stress control on x and z, we will impose strain rate on y
9  rate=-0.08
10 triax.stressMask = 5
11
12 triax.goal2=rate
13 triax.goal1=S_iso
14 triax.goal3=S_iso
15
16 def history():
17     plot.addData( e22=-triax.strain[1])
18     if (-triax.strain[1])>.25:
19         O.pause()
```

3.3.2 Monotonic undrained triaxial test

The procedure of the confining phase is the same as the drained case, the difference lies in the loading phase.

To simulate in the undrained condition, during the deviatoric loading phase, the constant volume method is often used in DEM modeling (Islam, 2021) by making the assumption that the particles and the fluid present inside the pores are incompressible. The method mainly consists of controlling the volume variation by applying strain rates in the vertical and horizontal direction, so the sample volume is kept constant. As the code below shows, in Line 27, Line 28 and Line 29 are defined the strain rates for every direction, where the strain rate values in axis X and Z are half of the vertical component value.

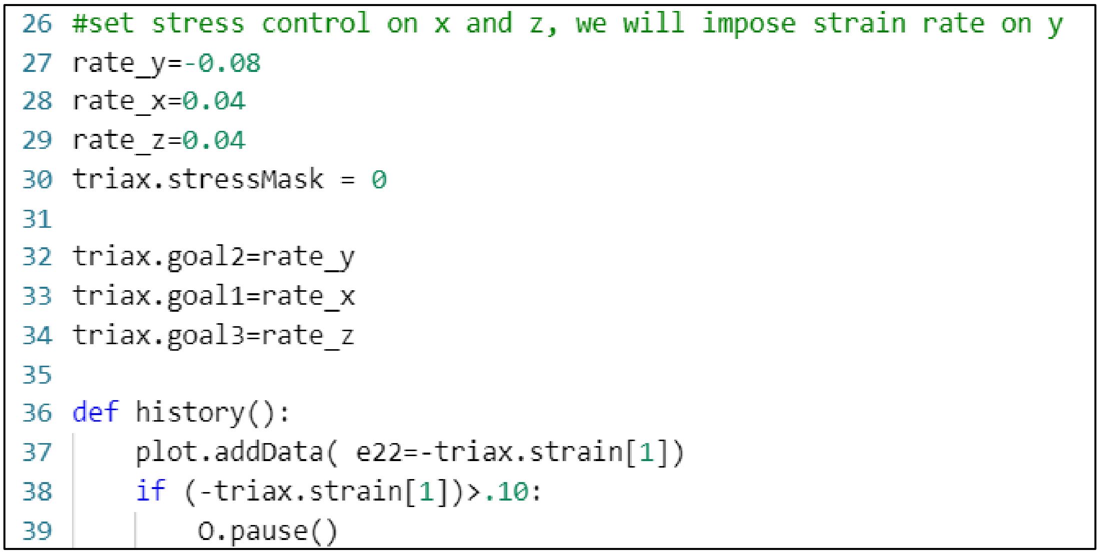

```
26 #set stress control on x and z, we will impose strain rate on y
27 rate_y=-0.08
28 rate_x=0.04
29 rate_z=0.04
30 triax.stressMask = 0
31
32 triax.goal2=rate_y
33 triax.goal1=rate_x
34 triax.goal3=rate_z
35
36 def history():
37     plot.addData( e22=-triax.strain[1])
38     if (-triax.strain[1])>.10:
39         O.pause()
```

In the Line 30 of the code above, the bitmask '*TriaxStressController.stressMask'* is set to zero, meaning that none of the goal values are stresses. In the Line 32, Line 33 and Line 34, the goal values for every direction are determined and shows that all of them are the strain rates defined before. The simulation ends once the axial strain defined in Line 38 is reached.

In this method, the change of volume of specimen and the void ratio should be very close to zero. However, the void ratio or porosity can have a small deviation due to the evolving of the granular structure during shear (Islam, 2021).

For samples with periodic boundaries, to apply the loading conditions, the engine '*PeriTriaxController'* is used. It also has a bitmask called *'stressMask'* which determines whether the imposed goal values are stresses or strain rates. The code below shows how the confining phase is defined.

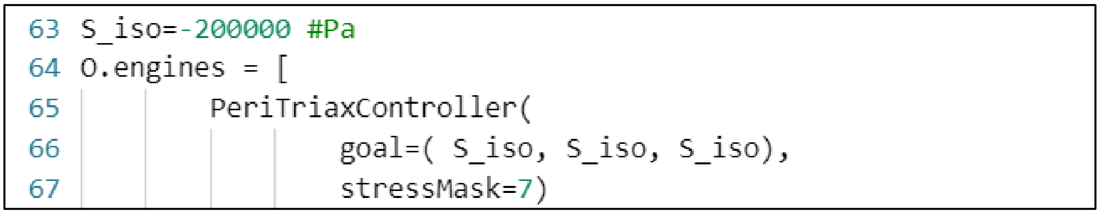

```
63 S_iso=-200000 #Pa
64 O.engines = [
65         PeriTriaxController(
66                 goal=( S_iso, S_iso, S_iso),
67                 stressMask=7)
```

During the deviatoric phase, the *‘stressMask’* is redefined as Line 73 shows. Due to the simulation is undrained and a constant volume is needed, the strain rate is used to set the goals.

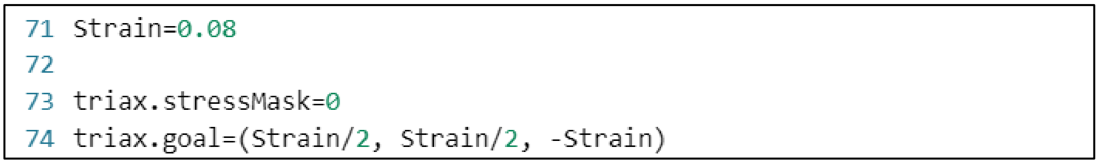

```
71 Strain=0.08
72
73 triax.stressMask=0
74 triax.goal=(Strain/2, Strain/2, -Strain)
```

3.3.3 Cyclic undrained triaxial test

The cyclic triaxial test is the most common laboratory method used in practice to evaluate the liquefaction response of soils (Basson, 2018).

After the confining phase, the constant volume is kept by controlling the strain rates in each direction, same as in the monotonic undrained test. The strain rates used in each direction are shown in Lines 43, 44 and 45 of the code below. In order to apply shear loading cycles a deviatoric stress amplitude q^{ampl} is specified, so the loading direction will switch by changing the sign of the strain rates once the specified value of deviatoric stress amplitude is reached.

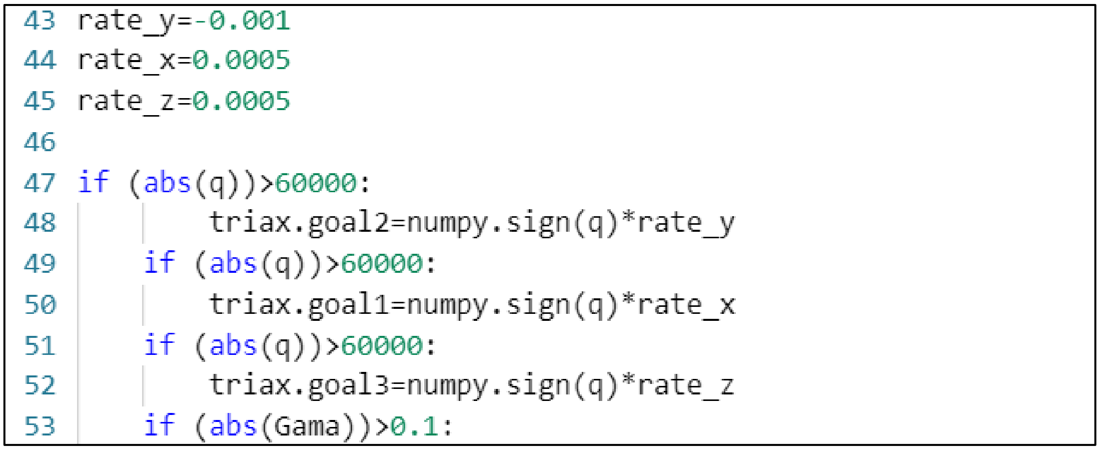

```
43 rate_y=-0.001
44 rate_x=0.0005
45 rate_z=0.0005
46
47 if (abs(q))>60000:
48         triax.goal2=numpy.sign(q)*rate_y
49     if (abs(q))>60000:
50         triax.goal1=numpy.sign(q)*rate_x
51     if (abs(q))>60000:
52         triax.goal3=numpy.sign(q)*rate_z
53     if (abs(Gama))>0.1:
```

In the above code, the loading direction is changed when $q = q^{ampl}$ =|60| kPa, redefining the goal values for each axis. At the vertical axis where there is compression will switch to extension and the two horizontal axes will switch from extension to compression as showed in Figure 3.5.

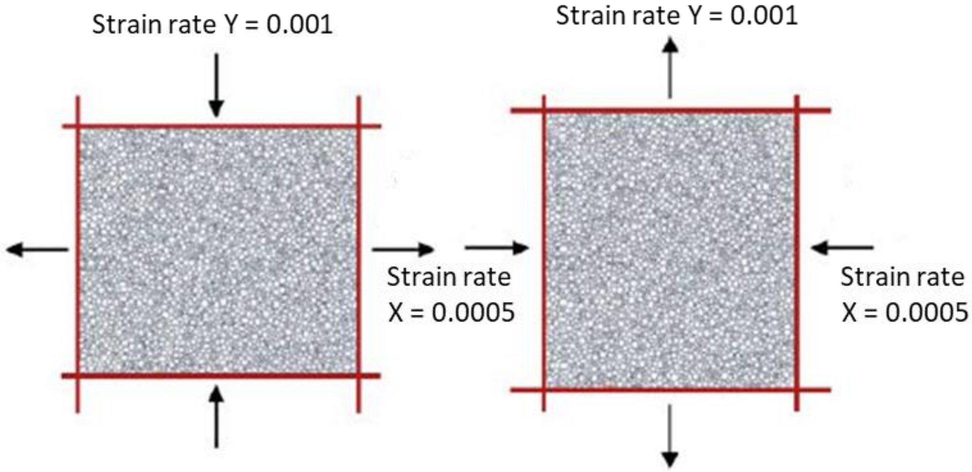

Figure 3.5: Scheme of the cyclic loading application on 2D sample (Wang et al., 2016).

3.3.4 Quasi-static condition

To check the quasi-static criterion, the inertial number I is calculated according to Equation 2-24 for the simulation conditions. Lopera Perez et al. (2016) proposed that the inertial number should be less than or equal to the upper limit of 2.5 x10^{-3} to ensure DEM simulations run under quasi-static regime. In this study, strain rates of 0.08, 0.05, 0.02 and 0.001 are used. The samples are compressed at a confining stress of 200 kPa and the density of the particle is 2650 kg/m^3. The mean diameter of the grains is 0.14 millimeters and the particle size distribution was multiplied in DEM by a scale factor of 70.

An example of Inertial number calculation for a strain rate of 0.08 is given below:

$$I = 0.08 * 70 * 0.14\ [mm] * 10^{-3} * \sqrt{\frac{2650\ \left[\frac{kg}{m^3}\right]}{200000\ [Pa]}} = 9.02\ x\ 10^{-5} \tag{3.2}$$

The Table 3.2 summarizes the I values obtained for each strain rate. As is can be seen, in all cases the inertial number is below the limit value.

Table 3.2: Inertial number for each strain rate used in the study.

$\dot{\varepsilon}$	I
0.001	1.13 E-06
0.02	2.26 E-05
0.05	5.64 E-05
0.08	9.02 E-05

3.3.5 Initial parameters

Molina (2022) proposed a set of contact law parameters to simulate the Karlsruhe fine sand behavior. These parameters showed a good correlation with the behavior under monotonic drained triaxial tests.

Table 3.3: Inertial Contact law parameters proposed by Molina (2022).

Parameter	Value
Contact stiffness E_c	400 [MPa]
Contact stiffness ratio v_c	0.3
Rotational stiffness k_r	0.05
Rotational coefficient η	0.25

These contact law parameters lead to obtain the maximum void ratio e_{max}=0.9 and the minimum e_{min}=0.67. In order to validate them, simulations of drained and undrained triaxial tests are carried out on samples isotropically compressed at 200 kPa (See Table 3.4 and Table 3.5). An inter particle-friction coefficient of 0.51 was applied.

Table 3.4: Program of drained monotonic triaxial compression tests according to Molina (2022) parameters.

EXPERIMENTAL SAMPLES			DEM SAMPLES		
	e_0	RD	Frictional coefficient	e_0	RD
TMD3	0.975	0.21	**0.287**	0.848	0.23
TMD13	0.824	0.63	**0.070**	0.737	0.70
TMD23	0.706	0.92	**0.035**	0.697	0.88

Table 3.5: Program of undrained monotonic triaxial compression tests according to Molina (2022) parameters.

EXPERIMENTAL SAMPLES			DEM SAMPLES		
	e_0	RD	Frictional coefficient	e_0	RD
TMU2	0.814	0.64	**0.105**	0.757	0.62

TMU5	0.946	0.29	**0.287**	0.848	0.23
TMU6	0.728	0.87	**0.070**	0.710	0.82

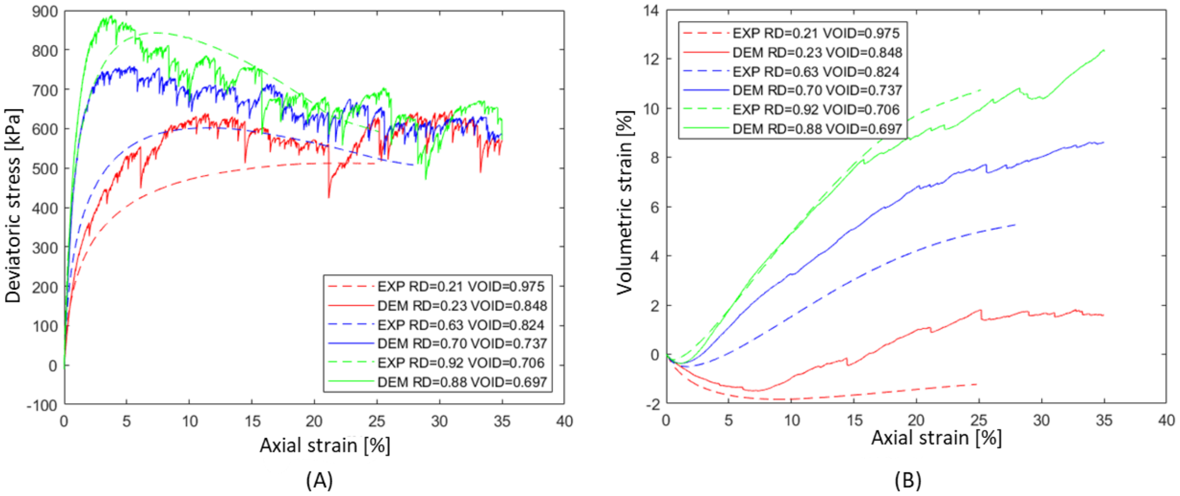

Figure 3.6: (A) Stress-strain curves and (B) volumetric behavior of soil samples prepared with Molina (2022) parameters subjected to triaxial test under drained conditions.

Although the loose and the medium dense specimen show a more dilative behavior than the experimental curves, the samples show a good match with the experiments overall, especially the dense specimen. Moreover, Figure 3.6 (A) shows the critical state is reached by all the specimens at an axial strain of approximately 30%.

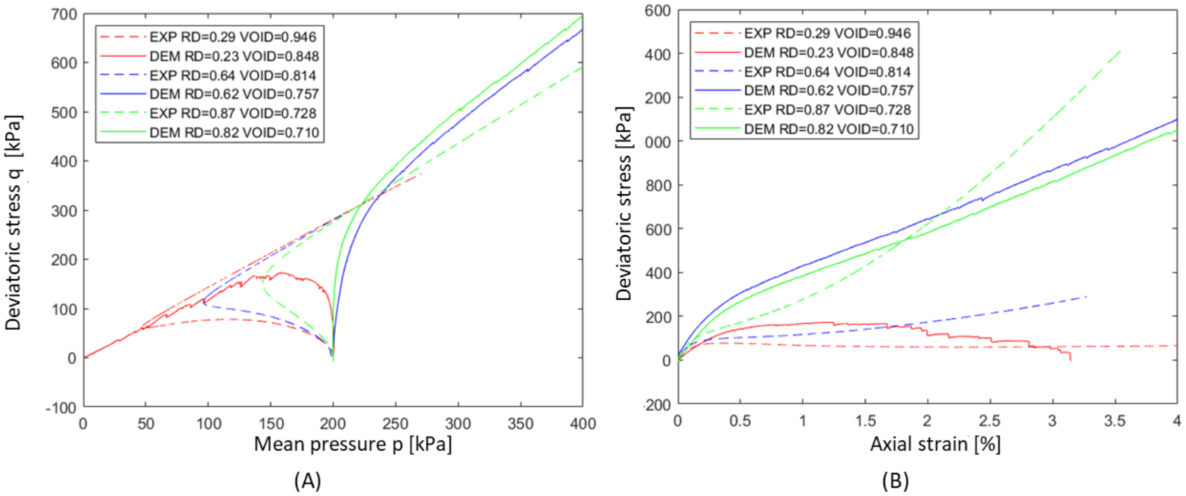

Figure 3.7: (A) Stress paths and (B) stress-strain relationship of soil samples prepared with Molina (2022) parameters subjected to triaxial test under undrained conditions.

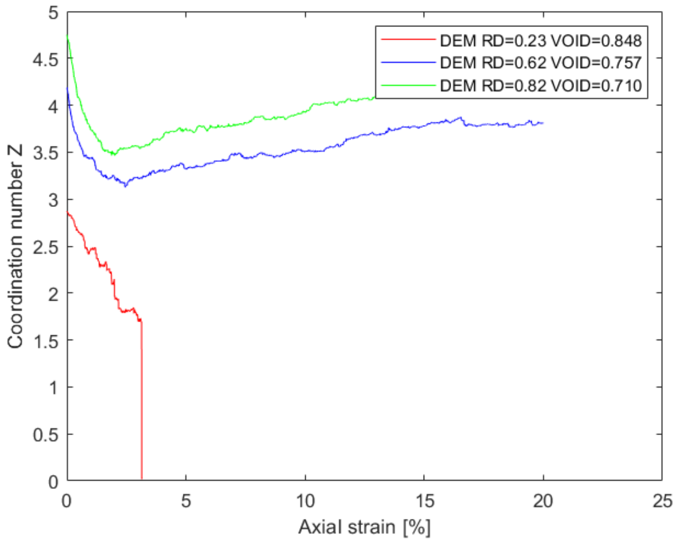

Figure 3.8: Coordination number of soil samples prepared with Molina (2022) parameters subjected to triaxial test under undrained conditions.

The samples with RD=0.82 and RD=0.62 do not present a good correlation with the experimental behavior: both of them show much stiffer response than the curves obtained experimentally. There is no loss of mean effective stress during simulation. On the other hand, Figure 3.7 (A) shows how the loose sample with RD=0.23 started losing effective stress as expected, but once the stress path finds the steady state line (SSL) loses all its strength at an axial strain value around 3%. (Figure 3.7 (B)). This behavior can also be observed in Figure 3.8, where the coordination number of the loose sample suddenly drops down to zero, meaning the specimen loses its resistant structure.

Since the proposed set of parameters does not validate the material behavior under undrained conditions, a recalibration is to be done in order to better capture Karlsruhe fine sand behavior.

3.3.6 Recalibration

Several researchers have studied the influence that each parameter of the contact model in DEM has on the material behavior under drained triaxial test conditions (Basson, 2018; Islam, 2021; Molina, 2021). Calibration of the contact model parameters is based on the trial-and-error method and the effect of each parameter was studied separately, by varying one parameter at the time while maintaining the rest constant.

The calibration process is as follows (Basson, 2018):

1. Provide nominal values to the parameters based on literature.
2. Calibrate the contact stiffness, which controls the initial response of the stress strain curve and macroscopic Young's modulus of the material.
3. Calibrate the contact stiffness ratio, which controls the initial volumetric response of the material.
4. Calibrate the rotational stiffness, which controls the dilation angle and volume change response.
5. Calibrate the rotational coefficient, which controls the peak stress in the stress strain curve.

Figure 3.9 shows the typical behavior of dense and loose samples in triaxial testing under drained conditions showing the influence of different contact parameters on the response of material.

Once the contact law parameter has been chosen, the relative density of the sample must be determined to check whether the combination of selected parameters need readjustment. Figure 3.10 shows a scheme of the calibration process.

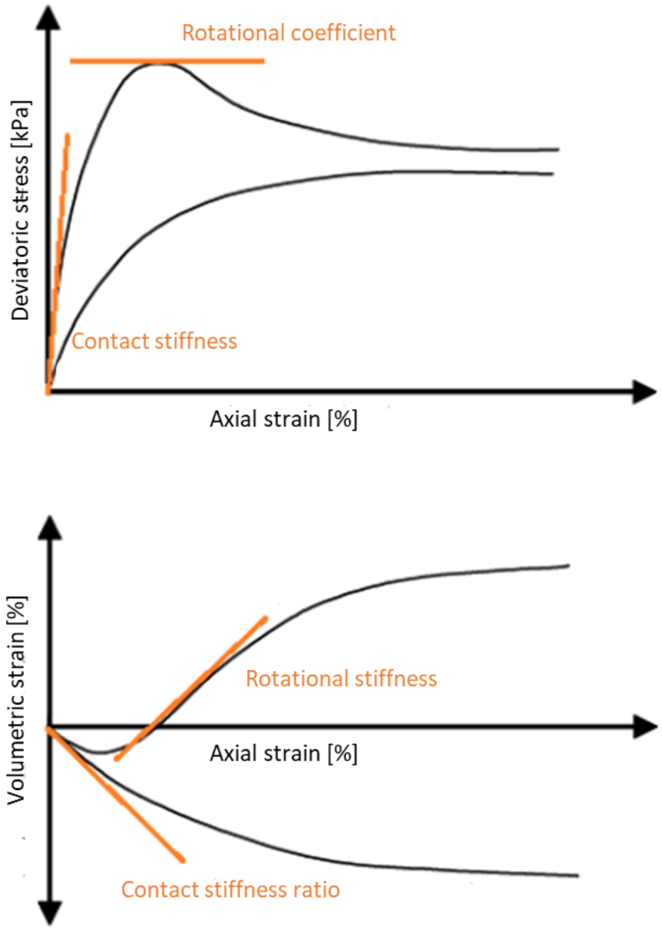

Figure 3.9: Typical behavior of samples in triaxial testing and the influence of contact parameters on response (Basson et al., 2020).

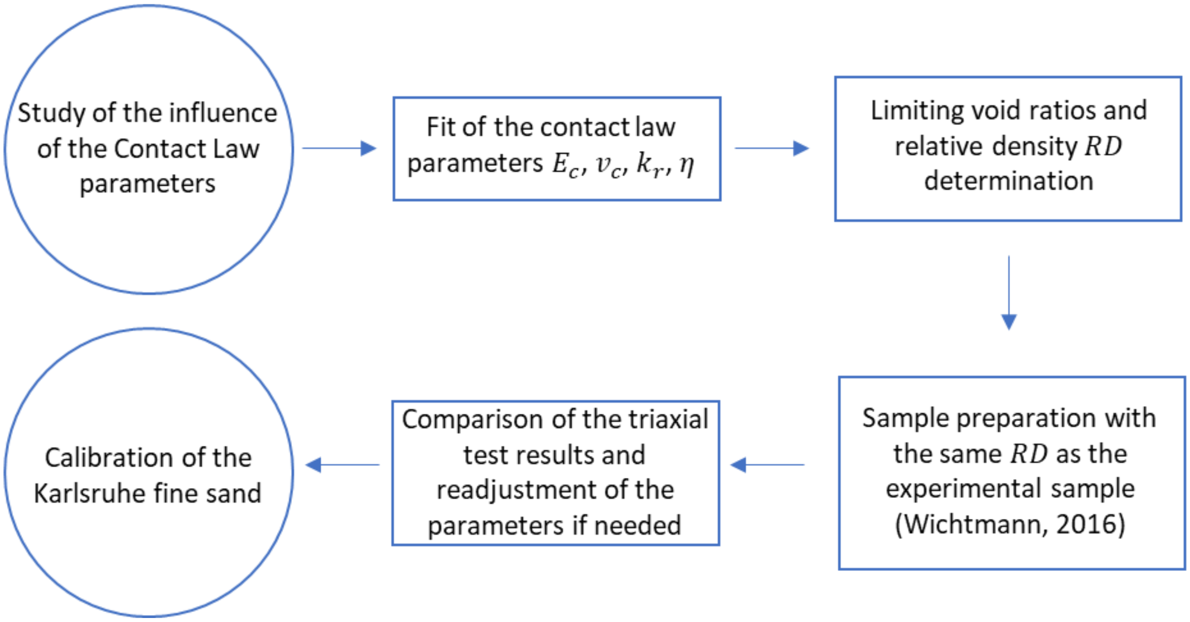

Figure 3.10: Calibration process of the material (Molina, 2021).

For the recalibration, cubic samples of length, width and height of 0.10 m with rigid boundaries are created using the process explained in Section 3.1 and isotropically compressed at a confining pressure of 200 kPa. Table 3.6 summarizes the selected new set of parameters for the Karlsruhe fine sand.

Table 3.6: New contact law parameters.

Parameter	**Value**
Contact stiffness E_c	200 [MPa]
Contact stiffness ratio v_c	0.3
Rotational stiffness k_r	0.05
Rotational coefficient η	0.25

The friction coefficient is adjusted as well to a value of 0.34. With these parameters, the maximum and minimum void ratio shown in Table 3.7 were obtained.

Table 3.7: Obtained maximum and minimum void ratio.

	e_{min}	e_{max}
Rigid boundaries	0.65	0.88

Once the samples are prepared at a given confining pressure, the relative density of each one is determined by means of the Equation 3.1.

Table 3.8: Program of drained monotonic triaxial compression tests according to recalibrated parameters using rigid boundaries.

EXPERIMENTAL SAMPLES			DEM SAMPLES	
	e_0	RD	e_0	RD
TMD8	0.859	0.52	0.752	0.55
TMD13	0.824	0.63	0.737	0.62
TMD23	0.706	0.92	0.664	0.94

Table 3.9: Program of undrained monotonic triaxial compression tests according to recalibrated parameters using rigid boundaries.

EXPERIMENTAL SAMPLES			DEM SAMPLES	
	e0	RD	**e0**	RD
TMU2	0.814	0.64	0.737	0.62
TMU5	0.946	0.29	0.803	0.32
TMU6	0.728	0.87	0.683	0.85

Table 3.10: Program of drained cyclic triaxial compression tests according to recalibrated parameters using rigid boundaries.

EXPERIMENTAL SAMPLES			DEM SAMPLES	
	e0	RD	**e0**	RD
TCUI7	0.8	0.67	0.723	0.68
			0.769	0.47
			0.803	0.32

In Table 3.8, Table 3.9 and Table 3.10 are summarized the experimental samples together with the corresponding numerical samples that are to be compared with under the following simulated tests: drained triaxial test with monotonic loading, undrained triaxial with monotonic loading and undrained triaxial test with cyclic loading .

Also, numerical samples to be tested under undrained conditions using periodic boundaries were prepared (See Table 3.11), in which the same frictional coefficient used on the samples with rigid boundaries was applied.

Table 3.11: Program of undrained monotonic triaxial compression tests according to recalibrated parameters using periodic boundaries.

EXPERIMENTAL SAMPLES			DEM SAMPLES	
	e0	RD	**Frictional coefficient**	**e0**
TMU2	0.814	0.64	**0.105**	0.64
TMU5	0.946	0.29	**0.176**	0.68
TMU6	0.728	0.87	**0.035**	0.55

3.4 Conclusions

The followed method for the modelling has been explained. The understanding of effect of each contact law parameter is primordial for an accurate calibration of the model, trying to approach the initial conditions and results obtained with the experimental samples. It is important to observe the behavior of the compression curves to set the initial conditions, according to the maximum and minimum void ratios.

CHAPTER 4 RESULTS AND DISCUSSIONS

4.1 Introduction

This chapter presents the results of each triaxial test modelled under different loading and drainage conditions. The obtained results were compared to the experimental results obtained by Wichtmann and Triantafyllidis (2016).

4.2 Monotonic drained triaxial test

The simulations were performed in samples with different relative densities, summarized in Table 3.8. The two loosest samples show good agreement with the experimental results obtained by Wichtmann and Triantafyllidis (2016) in the volumetric strain-axial strain plot (See Figure 4.1), while the densest sample shows a less dilative behavior than the experiment.

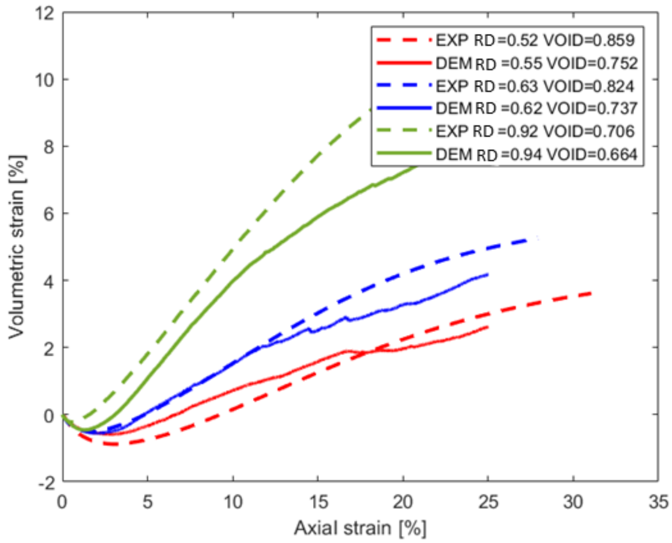

Figure 4.1: Volumetric behavior in drained monotonic triaxial tests performed on samples prepared different relative densities.

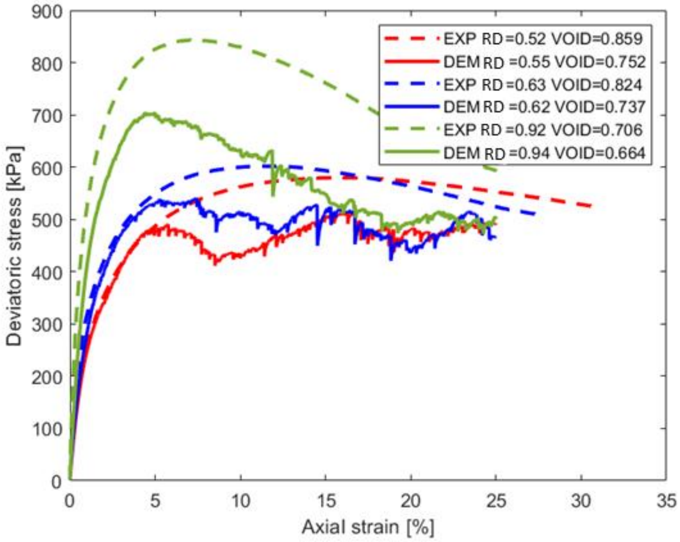

Figure 4.2: Stress-strain relationships measured in drained monotonic triaxial tests performed on samples prepared different relative densities.

In Figure 4.2 the stress-strain behavior is presented. The simulations curves of the three samples show a good adjustment with the experimental curves for low values of axial strain, underlining an adequate choice of the contact stiffness. However, the peak deviatoric stresses are still not well captured, especially for the densest sample.

For numerical simulations the critical state is reached at an axial strain close to 20% whereas in the experiment the critical state is possibly reached at an axial deformation of 30-35%. Nevertheless, both experiment and DEM simulations, achieve the same value of ultimate deviatoric strength.

4.3 Monotonic undrained triaxial test

4.3.1 Rigid boundaries

The numerical results obtained under monotonic undrained triaxial compression compared to the experiments are presented in Figure 4.3 and Figure 4.4. The behavior of the two numerical specimens with lower relative density show a good fit with the experimental response. The stress-strain curves showed in Figure 4.3 for samples with RD=0.35 and RD=0.62 have similar slopes to the experimental results and they reach a similar ultimate deviatoric strength. Contrariwise, this behavior is not observed in the sample with RD=0.88, as at the same ultimate axial strain, the numerical value of deviatoric stress is below the experimental curve.

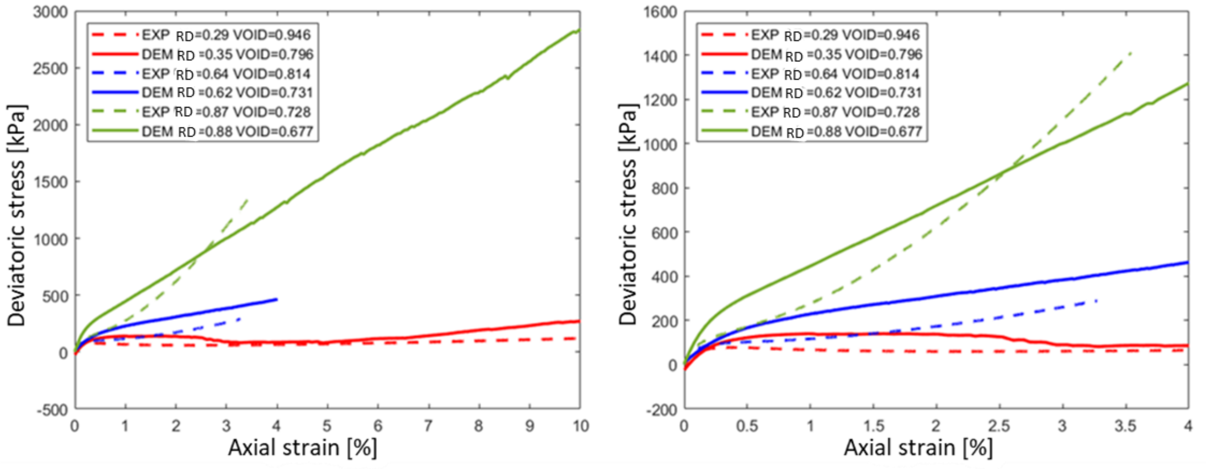

(A) (B)

Figure 4.3: (A) Stress-strain relationship measured in undrained monotonic triaxial tests with different relative densities and (B) zoomed version.

In Figure 4.4 the mean effective stress against deviatoric stress is plotted. The specimen with relative density of DR=0.35 shows a good adjustment with the experimental, the quasi-steady state (QSS) and the steady state line (SSL) slope are well achieved, even though the instability state (IS) point is not reached, as the deviatoric stress value, for the same pressure value, is higher than the experimental result. On the other hand, neither the sample with relative density RD=0.62 nor the sample with RD=0.88 reached the QSS or the IS point.

Figure 4.5 shows the variation of the coordination number along the simulation. It can be seen how the number of contacts of the sample with RD=0.35 drops to a very low value until it reaches the QSS point, and both coordination number and mean pressure begin to increase. Differently, the couple of densest samples once they reach the steady state line (SSL), the coordination number increase.

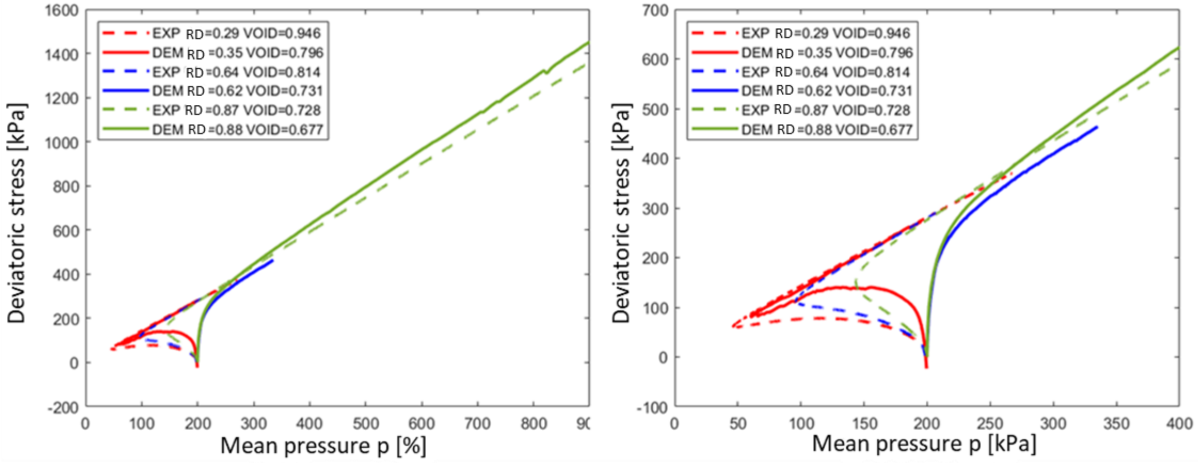

(A) (B)

Figure 4.4: (A) Stress path measured in undrained monotonic triaxial tests with different relative densities and (B) zoomed version.

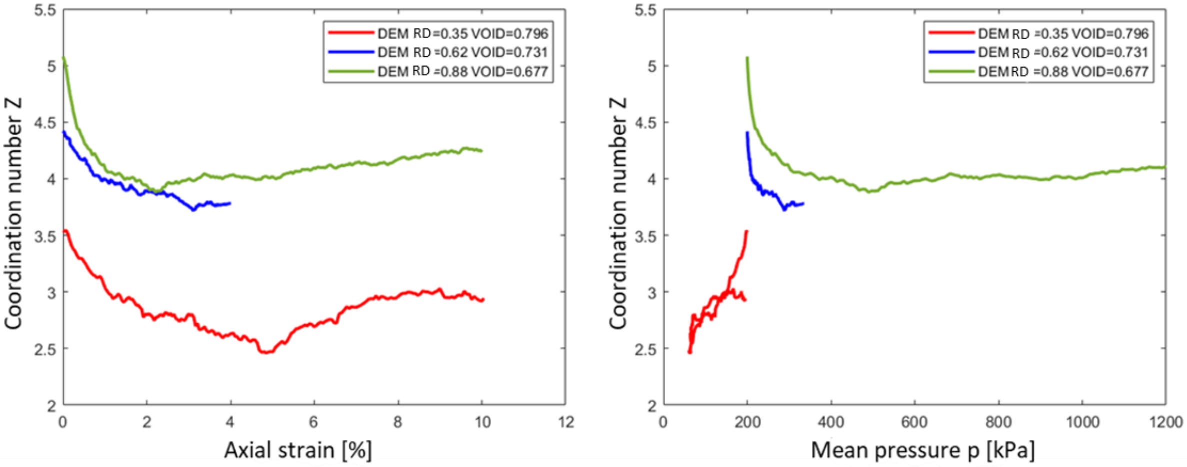

(A) (B)

Figure 4.5: Coordination number measured in undrained monotonic triaxial tests with different relative densities against (A) axial strain and (B) mean pressure.

Samples with similar relative density but compressed under different confining pressures have also been plotted in Figure 4.6 and Figure 4.7. In the stress-strain plot can be seen that the ultimate deviatoric stress and the slope of the sample compressed at 200 kPa is similar the experimental results, while the samples with higher confining pressures have an ultimate deviatoric stress value below the experimental curve. However, the Figure 4.7 shows that the specimen with highest confining pressure has a better adjustment than the other cases due to it shows some loss in the mean effective stress, approaching the experimental QSS. In addition, the three samples emulate the slope of the steady state line well. Figure 4.8 shows how the coordination number of the three specimens drops until they reach the SSL.

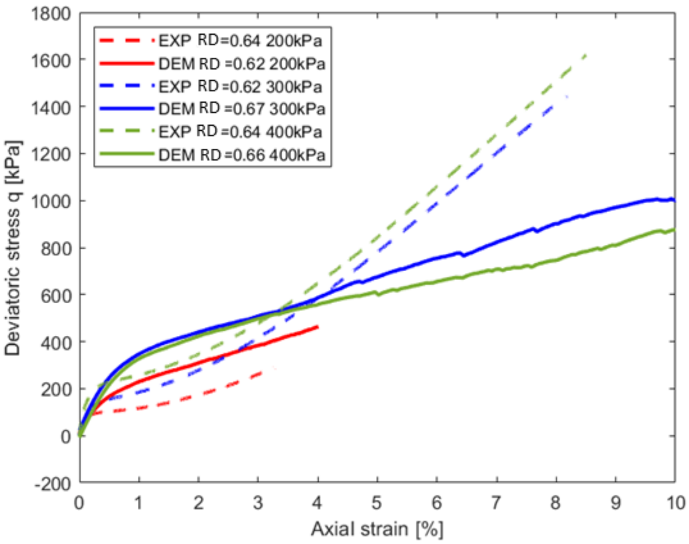

Figure 4.6: Stress-strain relationship measured in undrained monotonic triaxial tests with different confining pressures.

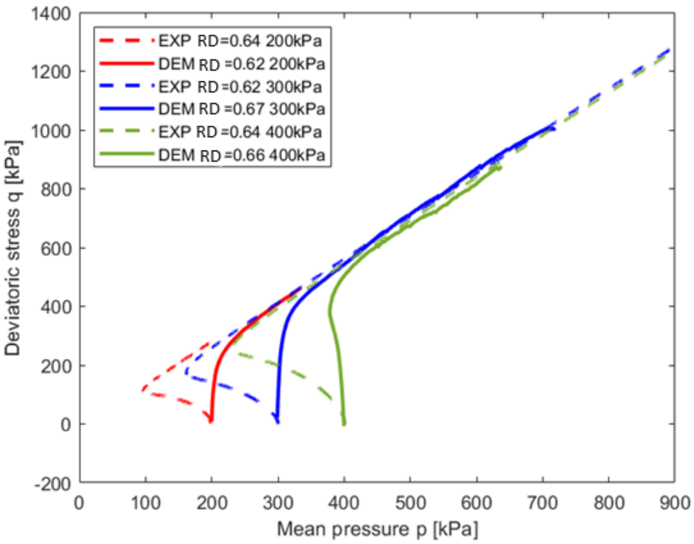

Figure 4.7: Stress path measured in undrained monotonic triaxial tests with different confining pressures.

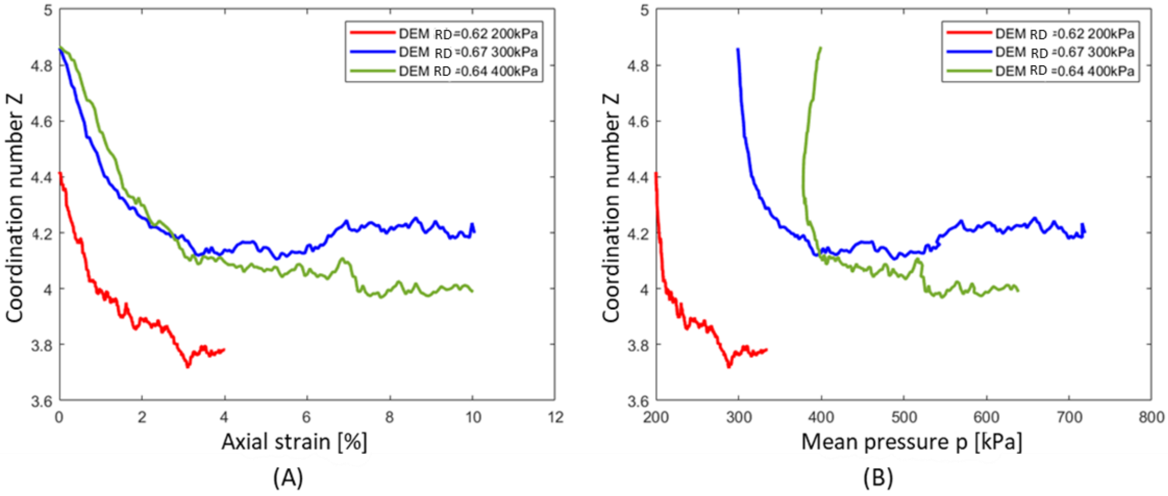

(A)

(B)

Figure 4.8: Coordination number measured in undrained monotonic triaxial tests with different confining pressures against (A) axial strain and (B) mean pressure.

4.3.2 Periodic boundaries

In Figure 4.9 and Figure 4.10, the results of tests on samples prepared with periodic boundary conditions (See Table 11) are compared with the experiment and results obtained from tests on samples with rigid boundaries. For the sample with RD=0.62, the deviatoric stress at the same ultimate axial strain of the experimental curve, is reached better than the sample prepared with rigid walls. Even though the stress-strain curve of the densest sample with periodic boundaries is now lower and do not reach the ultimate deviatoric stress, the adjustment to the initial part of the experimental curve is better than its equivalent with rigid boundaries.

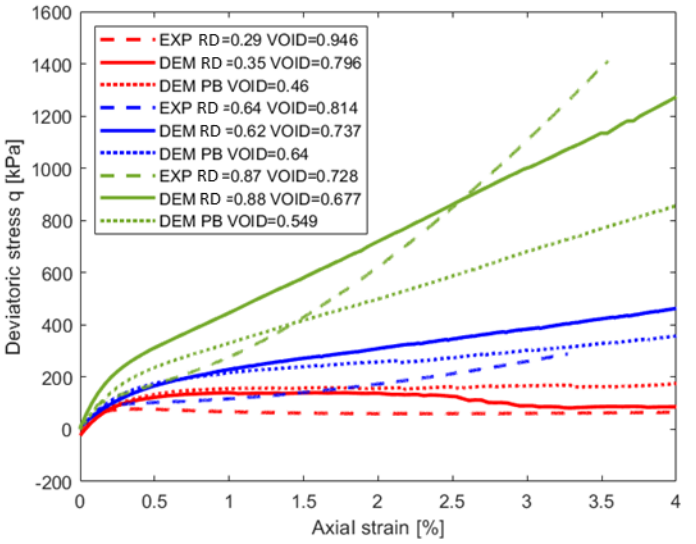

Figure 4.9: Stress-strain relationship measured in undrained monotonic triaxial tests with different confining pressures and periodic boundaries.

As shown in Figure 4.10, the loosest sample experienced some instability when is close to the steady state line and, even the specimen with RD=0.62 and periodic boundaries shows some approaching to the QSS of the experimental curve, they do not fully simulate the experimental behavior.

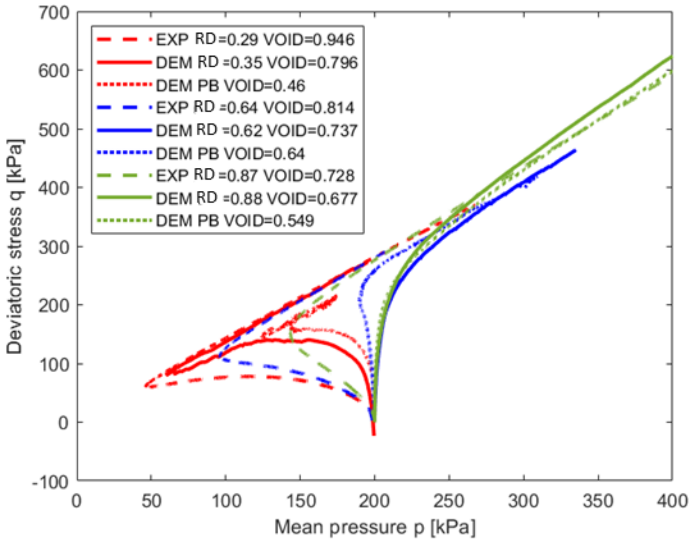

Figure 4.10: Stress path measured in undrained monotonic triaxial tests with different confining pressures and periodic boundaries.

4.4 Cyclic undrained triaxial test

The behavior of the samples showed in Table 3.10 tested under cyclic undrained triaxial compression is presented below. The samples with RD=0.68 and RD=0.47 do not experience liquefaction to be analyzed.

A loose sample with RD=0.32 was tested by applying stress cycles. It can be observed that the deviatoric stress values exceed the established limits (60 kPa), exposing a dynamic effect that is possibly due to the strain rate value. The sample presents a densification of loading cycles at the beginning of the simulation, but then the mean pressure decays per cycle are similar to the experimental results. Once the mean stress reaches zero, half a butterfly-like loop its generated, meaning that the sample reached the liquefaction state (See Figure 4.11).

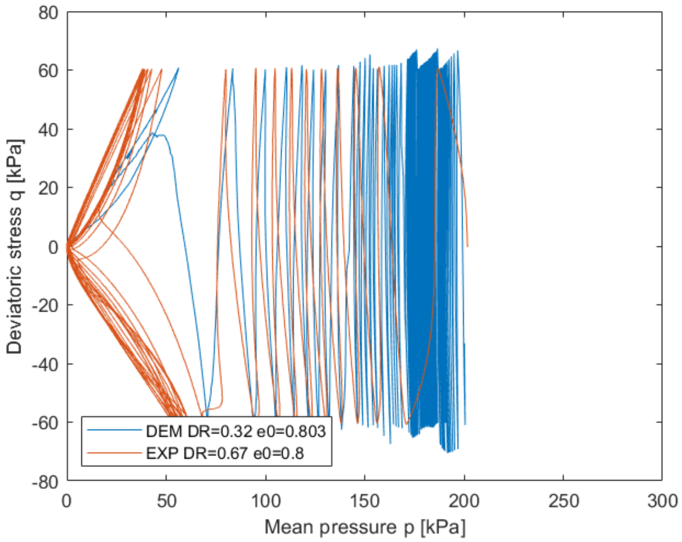

Figure 4.11: Stress path in undrained cyclic triaxial tests with isotropic initial stress and stress cycles performed on loose sample (RD=0.32).

Figure 4.12 shows how the axial strain of the numerical sample reach 8% approximately after one post-liquefaction cycle, which is larger the experimental results. That can be explained due to the difference of relative densities between both numerical and experimental samples.

In Figure 4.13 also can be seen the densification previously described. The simulation stars with a coordination number of 3.7 approximately, and for a large number of cycles it stays within the range of values [3.2 - 3.7]. The coordination number undergoes cyclic variations with an overall decreasing trend during pre-liquefaction loading. Once the coordination number drops below 1.9 the sample enters an instable state and will not regain effective stress until the coordination number exceed 1.9 again, indicating that the sample actually reached the liquefaction state and experienced deformation.

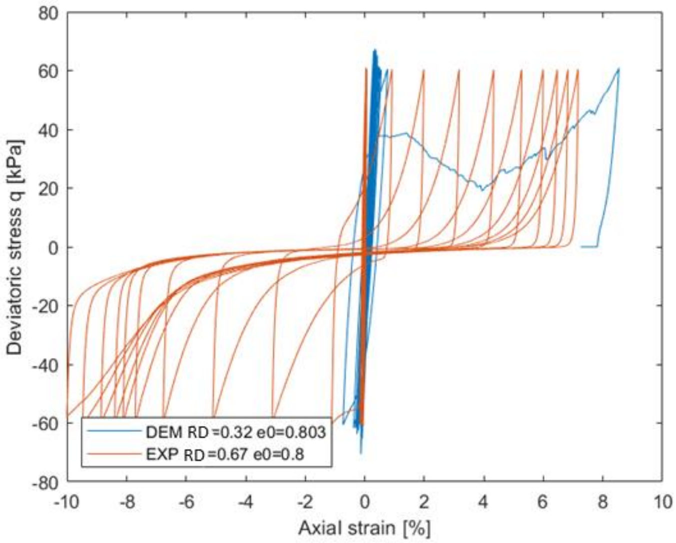

Figure 4.12: Stress-strain relationship in undrained cyclic triaxial tests with isotropic initial stress and stress cycles performed on loose sample (RD=0.32).

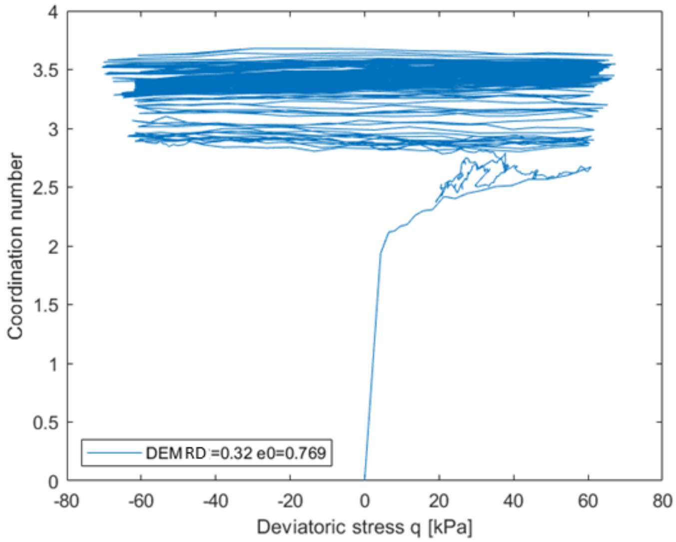

Figure 4.13: Coordination number against deviatoric stress in undrained cyclic triaxial tests with isotropic initial stress and stress cycles performed on loose sample (RD=0.32).

4.5 Conclusions

In this chapter, the results of the triaxial test modelling under different loading and drainage conditions were presented. DEM proved to be an appropriate tool to understand the micro-mechanical parameters. Numerical drained triaxial testing was able to replicate the dilative and contractive behavior. Under monotonic undrained loading conditions, the SSL slope is well resembled in all cases. In the simulations of undrained cyclic triaxial test did not show a significant relaxation in the mean effective stress. What remains for the future is to calibrate the rotational stiffness and rotational coefficient separately from the rest of the contact law parameters.

CHAPTER 5 CONCLUSIONS

This research aimed to study and evaluate the role microscopic parameters of a complex granular geometry play in the macroscopic behavior of Karlsruhe fine sand by means of DEM simulations of the triaxial test in both drained and undrained conditions under monotonic and cyclic loading.

Since the real material is idealized as a packing of spherical particles for sake of simplification, the introduction of contacts moments is needed to simulate the interlocking effect of the sand grains subangular shape. Numerical drained triaxial testing using calibrated parameters was able to replicate the dilative and contractive behavior and, at large deformation, the tested samples reach the critical state (q = 500 kPa), independent of the initial density. DEM proved to be an appropriate tool to understand the micro-mechanical parameters that affect the macroscopic stress-strain-volume change response of samples.

Simulations under monotonic undrained conditions were carried out with both rigid and periodic boundaries. In both cases, the two denser samples show an initial stiffer response than the experiment. However, the loosest sample resembled well the QSS of the experiment and both contractive and dilative tendencies can be observed. Although the ultimate deviatoric stress of the experiments is not reached by the dense sample, the SSL slope is well resembled in all cases.

In the simulations of undrained cyclic triaxial test, DEM samples with RD=0.68 and RD=0.47, did not show a significant relaxation in the mean effective stress, demonstrating the samples were far from liquefaction. It correlates with the results obtained in the monotonic undrained triaxial test with rigid boundaries, where the mean effective stress of the densest samples did not decrease or reach the QSS. However, the sample with RD=0.32 presented a gradual decrease of mean stress after each load cycle towards zero, facing a complete loss of shear strength during liquefaction.

The soil behavior under cyclic loading is correlated to the coordination number. The fabric parameter decreases with the increasing of number of cycles. It is annulled once the liquefaction is reached, allowing to evaluate the evolution of fabrics and identify a stability threshold below which the assembly has no longer a resistant structure.

Limiting void ratios were computed using isotropic compression and compared to the values reported in the literature. Although rotational law was used to simulate the angularity of the particles, limiting void ratios for DEM simulation were lower than the ones reported by Wichtmann and Triantafyllidis (2016); this evidences the inability to completely overcome the lack of use of the real shape of the grains.

In this study, an attempt of improving an existing calibration of the contact law parameters was done in order to validate it for different testing conditions. For further development, to calibrate the rotational stiffness and rotational coefficient separately from the rest of the contact law parameters would be convenient. This way there will be a general set of contact law parameters for the sand (contact stiffness E_c, contact stiffness ratio v_c, contact friction angle φ and density ρ) and a set of rotational parameters (rotational stiffness k_r and rotational coefficient η) trying to better simulate the interlocking effect of the sand grains for each loading and drainage conditions.

REFERENCES

Basson, M. S. (2018). Discrete element modelling of conventional geotechnical tests. Master's thesis. Indian Institute of Technology Delhi, 138 p.

Basson, M.S., Cudmani, R., Ramana, G.V. (2020). Evaluation of Macroscopic Soil Model Parameters Using the Discrete Element Method. In: Prashant, A., Sachan, A., Desai, C. (eds) Advances in Computer Methods and Geomechanics. Lecture Notes in Civil Engineering, vol 55. Springer, Singapore.

Been, K., Jefferies, M. G. (1985). A state parameter for sands. Géotechnique 35, 99–112.

Belheine, N., Plassiard, J. P., Donz´e, F. V., Darve, F., Seridi, A. (2009). Numerical simulation of drained triaxial test using 3D discrete element modeling. Computers and Geotechnics, 36(1-2), 320–331.

Braja, M. Das (2001). Fundamentos de Ingeniería Geotécnica. Ed Cengage Learning Latin Am.

Chareyre, B., Villard, P. (2005). Dynamic Spar Elements and Discrete Element Methods in Two Dimensions for the Modeling of Soil-Inclusion Problems. Journal of Engineering Mechanics, 131(7), 689–698.

Cundall, P.A. (1971). A computer model for simulating progressive, large-scale movement in blocky rock system. In Proceedings of the International Symposium on Rock Mechanics, 1971.

Cundall, P.A., Strack, O.D.L. (1979). A discrete numerical model for granular assemblies. Geotechnique 29, No. 1, 47-65.

Da Cruz, F., Emam, S., Prochnow, M., Roux, J. N., Chevoir, F. (2005). Rheophysics of dense granular materials: Discrete simulation of plane shear flows. Physical Review E - Statistical, Nonlinear, and Soft Matter Physics, 72(2).

Holtz, R. D., Kovacs, W. D. (1981). An Introduction to Geotechnical Engineering (733 p). Englewood Cliffs, NJ: Prentice Hall.

Ishihara, K. (1996). Soil Behaviour in Earthquake Geotechnics. Oxford engineering science series, ISSN 0953-3222, Oxford science publications.

Islam, S. (2021). DEM Simulation of Triaxial Behavior for Karlsruhe Fine Sand using Particle Flow Code. Master's thesis. University of Munich, 89 p.

Iwashita, K., M. Oda (1998). Rolling Resistance at Contacts in Simulation of Shear Band Development by DEM. Journal of Engineering Mechanics, 124(3), 285–292.

Janda, A., Ooi, J.Y. (2016). DEM modeling of cone penetration and unconfined compression in cohesive solids. Powder technology 293, 60-68.

Lopera Perez, J. C., Kwok, C. Y., Sullivan, C. O., Huang, X., Hanley, K. J. (2016). Assessing the Quasi-Static Conditions for Shearing in Granular Media within the Critical State Soil Mechanics Framework. Soils and Foundations 56(1):152–59.

Mitchell, J., Soga, K. (2005). Fundamentals of Soil Behavior. Wiley, New York.

Modenese, C., Utili, S., Houlsby, G. (2012). A Numerical Investigation of Quasi-static Conditions for Granular Media. Discrete Element Modelling of Particulate Media. The Royal Society of Chemistry, 2012, 187–195.

Molina, M.V. (2021). Análisis del comportamiento de suelos granulares aplicando el método de elementos discretos. Bachelor's thesis. Universidad Nacional de Tucumán, 93 p.

Molina, M.V. (2022). Personal communication.

Murthy, T. G., Loukidis, D., Carraro, J. A. H., Prezzi, M. & Salgado, R. (2007). Undrained monotonic response of clean and silty sands. Ge´otechnique 57, No. 3, 273–288

O'Sullivan, C., Bray, J. D. (2004). Selecting a suitable time step for discrete element simulations that use the central difference time integration scheme. Engineering Computations, 21(2/3/4), 278–303.

Rothenburg L., Bathurst R. J. (1992). Micromechanical features of granular materials with planar elliptical particles. Geotechnique, 42 (1), 79–95.

Seed, R., Cetin, K., Moss, R., Kammerer, A., Wu, J., Pestana, J., . . . Faris, A. (2003). Recent Advances in Soil Liquefaction Engineering: a Unified and Consistent Framework, Keynote Presentation. Long Beach, California: 26th Annual ASCE Los Angeles Geotechnical Spring Seminar.

Sladen, J. A., D' Hollander, R. D., Krahn, J. (1985). The liquefaction of sands, a collapse surface approach. Can. Geotech. 1. 22 4, 564– 578.

Šmilauer, V. et al. (2021). Yade Documentation 3rd ed. The Yade Project.

Taylor, D. (1948). Fundamentals of Soil Mechanics. John Wiley & Sons, New York.

Thornton, C. (2000). Numerical simulations of deviatoric shear deformation of granular media. Géotechnique (50), pages 43–53.

Tsukamoto, Y., Ishihara, K. (2022). Advances in soil liquefaction engineering. Springer Singapore.

Wang, G., Wei, J. (2016) Microstructure evolution of granular soils in cyclic mobility and post-liquefaction process. Granular Matter 18, 51.

Wang, R., Fu, P., Zhang, JM. et al. (2016). DEM study of fabric features governing undrained post-liquefaction shear deformation of sand. Acta Geotech. 11, 1321–1337.

Wichtmann, T., Triantafyllidis, Th. (2016). An experimental data base for the development, calibration and verification of constitutive models for sand with focus to cyclic loading. Part

I: tests with monotonic loading and stress cycles. Acta Geotechnica, Vol. 11, No. 4, pp. 739-761.

Widulinski, Ł., Kozicki, J., Tejchman, J. (2009). Numerical simulations of triaxial test with sand using DEM. Archives of Hydroengineering and Environmental Mechanics, 56(3-4), 149–172.

Zhang, L., Evans, T.M., 2018. Boundary effects in discrete element method modeling of undrained cyclic triaxial and simple shear element tests. Granular Matter 20 (4), 60.

Zhao, X., Evans, T.M. (2011). Numerical Analysis of Critical State Behaviors of Granular Soils under Different Loading Conditions. Granular Matter, 13, 751-764.

UNIVERSIDAD DE CONCEPCIÓN – FACULTAD DE INGENIERÍA
RESUMEN DE MEMORIA DE TÍTULO

Departamento	**:** Departamento de Ingeniería Civil
Carrera	**:** Ingeniería Civil
Nombre del memorista	: Margarita León Arriagada
Título de la memoria	**:** Numerical simulation of the dynamic response of granular soils by means of the discrete element method (DEM)
Fecha de la presentación oral	**:**
Profesor(es) Guía	**:** Gonzalo Montalva
Profesor(es) Revisor(es)	**:** Daniella Escribano
Concepto	**:**
Calificación	**:**

Resumen

Numerical methods are being implemented widely in geotechnical engineering; however, methods based on continuum mechanics are not able to provide microscale level information. Discrete Element Method (DEM) discretize the space into discrete particles and, through the analysis of micromechanical parameters that define the contact model, macroscopic behavior can be studied. DEM can capture the information at the particle level, and it has proven to be a valuable tool in the analysis of static and cyclic behavior of soils. In this study, an attempt of improving an existing calibration of the contact law parameters for Karlsruhe fine sand has been made to validate it for different testing conditions using DEM. Samples are prepared at target relative density and two types of boundary conditions are applied to explore its effect on DEM simulation. The contact law parameters for the sand are recalibrated based on the experimental results of Wichtmann and Triantafyllidis (2016). Under drained conditions, the numerical samples are able to replicate the volumetric change behavior, the dilative and contractive behavior and the initial stiffness of the experiment. The undrained behavior is examined by applying a constant volume method, where for the loose state there is a good agreement with the experimental results. Cyclic undrained results for dense samples correlates with the outcomes obtained under monotonic undrained conditions, showing a stiffer response than the experiment.